Theoretical analysis of the conductance histograms and structural properties of Ag, Pt and Ni nanocontacts

F. Pauly,[1,2,*] M. Dreher,[3] J.K. Viljas,[1,2] M. Häfner,[1,2] J.C. Cuevas,[1,2,4] and P. Nielaba[3]

[1] *Institut für Theoretische Festkörperphysik, Universität Karlsruhe, D-76128 Karlsruhe, Germany*
[2] *Forschungszentrum Karlsruhe, Institut für Nanotechnologie, D-76021 Karlsruhe, Germany*
[3] *Fachbereich Physik, Universität Konstanz, D-78457 Konstanz, Germany*
[4] *Departamento de Física Teórica de la Materia Condensada C-V, Universidad Autónoma de Madrid, E-28049 Madrid, Spain*

Conductance histograms are a valuable tool to study the intrinsic conduction properties of metallic atomic-sized contacts. These histograms show a peak structure, which is characteristic of the type of metal under investigation. Despite the enormous progress in the understanding of the electronic transport in metallic nanowires, the origin of this peak structure is still a basic open problem. In the present work we tackle this issue, extending our theoretical analysis of Au conductance histograms [Dreher *et al.*, PRB **72**, 075435 (2005)] to different types of metals, namely, Ag, Pt and ferromagnetic Ni. We combine classical molecular dynamics simulations of the breaking of nanocontacts with conductance calculations based on a tight-binding model. This combination gives us access to crucial information such as contact geometries, strain forces, minimum cross-sections, the conductance, transmissions of the individual conduction channels and, in the case of Ni, the spin polarization of the current. We shall also briefly discuss investigations of Al atomic-sized contacts. From our analysis we conclude that the differences in the histograms of these metals are due to (i) the very different electronic structures, which means different atomic orbitals contributing to the transport, and (ii) the different mechanical properties, which in a case like Pt lead to the formation of special structures, namely monoatomic chains. Of particular interest are results for Ni that indicate the absence of any conductance quantization, and show how the current polarization evolves (including large fluctuations) from negative values in thick contacts to even positive values in the tunneling regime after rupture of the contact. Finally, we also present a detailed analysis of the breaking forces of these metallic contacts, which are compared to the forces predicted from bulk considerations.

PACS numbers: 73.63.-b, 73.63.Rt, 73.23.-b, 73.40.Jn

I. INTRODUCTION

The transport properties and mechanical characteristics of metallic atomic-scale wires have been the subject of numerous studies over the past years.[1] The analysis of these nanocontacts is nowadays possible due to experimental techniques like the scanning tunneling microscope[2,3] and mechanically controlled break junctions.[4] In both cases a metallic contact is stretched with a precision of a few picometers by the use of piezoelectric elements, providing very detailed information about the formation and breaking of metallic systems at the nanoscale.

The relative simplicity of these nanowires makes them ideal systems to perform extensive comparisons with microscopic theories. Such comparisons have allowed, in particular, to elucidate the nature of electrical conduction. The conduction in such systems is usually described in terms of the Landauer formula, according to which the low-temperature linear conductance of nonmagnetic contacts can be written as $G = G_0 \sum_n T_n$, where the sum runs over all the available conduction channels, T_n is the transmission for the nth channel and $G_0 = 2e^2/h$ is the quantum of conductance. As was shown in Ref. 5, the set of transmission coefficients is amenable to measurement in the case of superconducting materials. Using this possibility it has been established that the number of channels in a one-atom contact is determined by the number of valence orbitals of the central atom, and the transmission of each channel is fixed by the local atomic environment.[6,7,8]

The experiments show that in the stretching processes in which these metallic wires are formed, the conductance evolves in a step-like manner which changes from realization to realization. In order to investigate the typical values of the conductance, different authors introduced conductance histograms, constructed from a large number of individual conductance curves.[9,10,11] These histograms often show a peak structure, which is specific to the corresponding metal. Thus for instance, for noble metals like Au and Ag and for alkali metals like sodium, the conductance has a certain preference to adopt multiples of G_0. However, for a large variety of metals, the peaks do not appear at multiples of G_0 (for a detailed discussion of the conductance histograms, see section V.D in Ref. 1). It has become clear that the peak structure in the conductance histograms must be related to the interplay between electronic and mechanical properties. This interplay was nicely illustrated in the first simultaneous measurement of the conductance and breaking force,[12] but the precise origin of the differences between the various classes of metals remains to be understood. The solution of this basic open problem is precisely the central goal of the present work.

The analysis of the characteristic peaks of the conductance histograms of alkali and noble metals at relatively high temperatures has revealed the existence of exceptionally stable radii arising from electronic shell effects for thin wires and atomic shell effects for thicker wires.[13,14,15,16,17] Stable nanowires with thicknesses of several atoms could also be observed in transmission electron images.[18,19,20] Commonly, the connection between the peaks in the conductance histograms and the radius of the contacts is established using semiclassical arguments based on the Sharvin formula or slight variations of it[21]

$$G = G_0 \left[\left(\frac{k_F R}{2} \right)^2 - \frac{k_F R}{2} + ... \right], \qquad (1)$$

where k_F is the Fermi wave vector and R is the radius of the wire.[22] Using this type of formula, it was suggested in Ref. 23 that peaks found in the histogram of the minimum cross-section (MCS) of Al contacts would immediately translate into peaks in the conductance histograms. In other words, it was suggested that the conductance peaks would just be a manifestation of the existence of certain particularly stable contacts.

From the theory side, the analyses of the conductance histograms are scarce in the literature. Mostly single stretching events have been investigated at various levels of sophistication.[24,25,26,27,28,29,30,31,32,33,34,35] The analysis of conductance histograms, however, involves the statistical exploration of many different stretching events. Most such research is based on free-electron models, where particular nanowire dynamics are chosen,[36] but there are practically no fully atomistic investigations of the conductance histograms. Two such studies have just recently appeared, where Dreher *et al.*[37] investigated atomic Au contacts and Hasmy *et al.*[38] studied Al contacts. In particular, in our work (Ref. 37) we showed that, at least at low temperatures (4.2 K), there is no simple correspondence between the first peaks in the MCS and the conductance histograms.

In order to elucidate the origin of the peak structure in the conductance histograms of metallic atomic-sized contacts, we have extended our theoretical analysis of the Au conductance histogram[37] to several new metals with varying electronic structures in the present work. In particular, we have studied the cases of Ag, a noble metal, Pt, a transition metal, and Ni, a ferromagnetic metal. We shall also briefly comment on our study of Al (an *sp*-like metal). Our theoretical approach is based on a combination of classical molecular dynamics (MD) simulations to describe the contact formation and a tight-binding (TB) model supplemented with a local charge neutrality condition for the atomistic computation of the conductance. This combination allows us to obtain detailed information on the mechanical and transport properties such as contact geometries, strain forces, the MCS, the conductance, the number and evolution of individual conductance channels and, in the case of ferromagnetic contacts, the spin polarization of the current.

Concerning Ag, we find a sharp peak in the conductance histogram at $1\,G_0$. This peak is due to the formation of single-atom contacts and dimers in the last stages of the breaking of the wires in combination with the fact that the transport in the noble metal is dominated by the *s* orbitals around the Fermi energy. With *single-atom contacts* we will refer throughout this article to junctions with a single atom in the narrowest constriction, in short a one-atom chain, while *dimer* means an atomic chain consisting of two atoms. In the case of Pt, the first peak is broadened and shifted to a higher conductance value (above $1\,G_0$). This is due to the fact that in this transition metal the *d* orbitals play a fundamental role in the transport, providing extra conduction channels, as compared to Ag. For Ni wires, we see that the *d* orbitals contribute decisively to the electrical conduction for the minority-spin component, providing several partially open channels even in the last stages of the stretching process. As a consequence, we do not observe any type of conductance quantization. With respect to the polarization of the current, we see that there is a crossover from large negative values for thick contacts contacts to positive values in the tunneling regime, right after the rupture of the contact.

From a more general point of view, the ensemble of our results allows us to conclude that the differences in the peak structure of the conductance histograms of metallic nanocontacts can be traced back to the following two ingredients. First, due to the different electronic structure of the various classes of metals different atomic orbitals contribute to the transport. These orbitals determine in turn the number of conducting channels and therefore the conductance values. Thus, for similar structures a contact of a multivalent metal will have in general a higher conductance than one of a noble metal. Second, the different mechanical properties give rise to the formation of certain characteristic structures, which are finally reflected in the histograms. For instance, the formation of monoatomic chains in Au or Pt is responsible for the pronounced last conductance peak.

The rest of this paper is organized as follows. In Sec. II we present the details of our method for simulating the stretching of atomic wires and show how the conductance is subsequently computed. Studies of Ag, Pt, Al and Ni contacts follow in Secs. III, IV, V and VI, respectively. In each of these sections we first discuss representative examples of the stretching processes of the nanocontacts. We then turn to the statistical analysis of the whole set of simulations for the different metals. This includes a discussion of the histograms of both the MCS and the conductance as well as an analysis of the mean channel transmission. Section VII is devoted to the discussion of the mechanical properties of the different metals. Finally, we summarize the main conclusion of this work in Sec. VIII.

II. THE THEORETICAL APPROACH

The goal of this study is the theoretical description of the mechanical and electrical properties of metallic nanojunctions. For this purpose, we make use of the approach introduced in our previous work on the conductance histogram of Au atomic contacts.[37] In order to analyze ferromagnetic Ni contacts, we need to extend our method to study also spin-dependent metals. Such an extension is presented below, but we refer the reader also to Ref. 37 for supplementary information.

Our theoretical method is based on a combination of classical MD simulations for the determination of the structure and mechanical properties of the nanowires and conductance calculations based on a TB model. We proceed to explain these two types of calculations in the next subsections.

A. Structure calculations

The breaking of metallic nanocontacts is simulated by means of classical MD simulations. In all our calculations we assume an average temperature of 4.2 K, which is maintained in the simulations by means of a Nosé-Hoover thermostat. The forces are calculated using semiempirical potentials derived from effective-medium theory (EMT).[39,40] This theory has already been successfully used for simulating nanowires.[32,41,42] For the starting configuration of the contacts we choose a perfect fcc-lattice of 112 atoms of length 2.65 nm (Ag), 2.55 nm (Pt), 2.64 nm (Al) and 2.29 nm (Ni) oriented along the [001] direction (z direction) with a cross-section of 8 atoms. This wire is attached at both ends to two slabs that are kept fixed, each consisting of 288 atoms. After equilibration, the stretching process is simulated by separating both slabs symmetrically by a fixed distance in every time step (1.4 fs). Different time evolutions of the nanocontacts are obtained by providing the 112 wire atoms with random starting velocities. The stretching velocity of 2 m/s is much bigger than in the experiment, but it is small compared with the speed of sound in the investigated materials (of more than 2790 m/s). Thus the wire can re-equilibrate between successive instabilities, while collective relaxation processes may be suppressed.[26,28]

In order to test whether the conductance changes are correlated with atomic rearrangements in the nanocontact, we calculate the radius of the MCS perpendicular to the stretching direction as defined by Bratkovsky *et al.*[27]

Finally, during the stretching process, every 1.4 ps a configuration is recorded and the strain force of the nanocontact is computed following Finbow *et al.*[43] Every 5.6 ps the corresponding conductance is calculated using the method described below.

B. Conductance calculations

We compute the conductance within the Landauer approach. To calculate the electronic structure of our atomic contacts a TB model is employed, which has been successful in describing the important qualitative features in the transport through metallic nanojunctions.[6,8,37] This model is based on the following Hamiltonian written in a nonorthogonal local basis

$$\hat{H} = \sum_{i\alpha,j\beta,\sigma} H_{i\alpha,j\beta,\sigma} \hat{c}^{\dagger}_{i\alpha,\sigma} \hat{c}_{j\beta,\sigma}, \qquad (2)$$

where i and j run over the atomic sites, α and β denote different atomic orbitals and $H_{i\alpha,j\beta,\sigma}$ are the on-site ($i = j$) or hopping ($i \neq j$) elements, which are spin-dependent ($\sigma = \uparrow, \downarrow$) in the case of ferromagnetic metals like Ni. Additionally, we need the overlap integrals $S_{i\alpha,j\beta}$ of orbitals at different atomic positions.[44] We obtain the quantities $H_{i\alpha,j\beta,\sigma}$ and $S_{i\alpha,j\beta}$ from a parameterization that is designed to accurately reproduce the band structure of bulk materials.[45,46] The atomic basis is formed by 9 valence orbitals, namely the s, p and d orbitals which give rise to the main bands around the Fermi energy. In this parameterization both the hoppings and the overlaps to a neighboring atom depend on the interatomic position, which allows us to apply this parameterization in combination with the MD simulations. The overlap and hopping elements have a cutoff radius that encloses up to 9 (Ag, Pt and Al) or 12 (Ni) nearest-neighbor shells. The left (L) and right (R) electrodes are constructed such that all the hopping elements from the 112 wire atoms, which we will call the central part or center of our contact (C), to the electrodes are taken into account. This means that the electrodes in the conductance calculation are constituted of [001] layers containing even more than the 288 slab atoms used in the structure calculations. Note that with the word electrode we will refer, throughout this article, to the fixed slab atoms (or the extended [001] layers used in the conductance calculations).

The local environment in the neck region is very different from that in the bulk material for which the TB parameters have been developed. This can cause large deviations from the approximate local charge neutrality that typical metallic elements must exhibit. Within the TB approximation we correct this effect by imposing a local charge neutrality condition on the atoms in the central part of the nanowire through a self-consistent variation of the Hamiltonian. This self-consistent procedure requires the computation of the electronic density matrix $P_{i\alpha,j\beta}$, which is obtained by integrating the Green function of the center up to the Fermi energy[47]

$$\hat{P}_{i\alpha,j\beta} = -\frac{1}{\pi} \int_{-\infty}^{E_F} \mathrm{Im} \left[\sum_{\sigma} \hat{G}^{r}_{CC,\sigma}(E) \right] dE. \qquad (3)$$

In this expression $\hat{G}^{r}_{CC,\sigma}$ is the retarded Green's function

of the central part of the contact

$$\hat{G}^r_{CC,\sigma}(E) = \left[E\hat{S}_{CC} - \hat{H}_{CC,\sigma} - \hat{\Sigma}^r_{L,\sigma} - \hat{\Sigma}^r_{R,\sigma}\right]^{-1}, \quad (4)$$

where σ stands for the spin component, $\hat{S}_{CC}$ is the overlap matrix of the center, $\hat{H}_{CC,\sigma}$ is the Hamiltonian and $\hat{\Sigma}_{X,\sigma}$ (with $X = L$ or R) are the self-energies that describe the coupling of the center to the electrodes. They are given by

$$\hat{\Sigma}^r_{X,\sigma}(E) = \left(\hat{H}_{CX,\sigma} - E\hat{S}_{CX}\right)\hat{g}^r_{XX,\sigma}\left(\hat{H}_{XC,\sigma} - E\hat{S}_{XC}\right), \quad (5)$$

with the unperturbed retarded electrode Green's function $\hat{g}^r_{XX,\sigma}$ and the overlap (hopping) matrices from the center to the electrodes $\hat{S}_{CX}$ ($\hat{H}_{CX,\sigma}$). The unperturbed electrode Green's functions are assumed to be bulk Green's functions in all our calculations. The charge on the atom i is then determined using a Mulliken population analysis

$$N_i = \sum_\alpha \left(\hat{P}_{CC}\hat{S}_{CC}\right)_{i\alpha,i\alpha}, \quad (6)$$

where only the contributions of the central part to the atomic charge are considered.[48,49] The new Hamiltonian matrix elements $H_{i\alpha,j\beta,\sigma}$ are obtained from the original ones $H^{(0)}_{i\alpha,j\beta,\sigma}$ as[50]

$$H_{i\alpha,j\beta,\sigma} = H^{(0)}_{i\alpha,j\beta,\sigma} + S_{i\alpha,j\beta}\frac{\phi_i + \phi_j}{2}. \quad (7)$$

The shifts ϕ_i are determined such that no atom deviates from the charge neutrality by more than 0.02 electron charges ($|N_i - N_{\rm atom}| < 0.02$, and $N_{\rm atom}$ stands for the electronic charge of the respective charge-neutral metal atom). Note that there is one shift parameter per central atom, also in the case of ferromagnetic metals.

The low-temperature linear conductance is then computed using a Green's function formalism (see Ref. 37 for details), finally resulting in the Landauer formula

$$G^\sigma(E_F) = \frac{e^2}{h}\sum_n T^\sigma_n(E_F) \quad (8)$$

with the Fermi energy E_F and the transmission T^σ_n of the nth transmission eigenchannel. The conductance is then given as the sum over the different spin contributions

$$G = \sum_\sigma G^\sigma, \quad (9)$$

which has the form

$$G = G_0 T(E_F) = G_0 \sum_n T_n \quad (10)$$

for the spin independent case. As explained in the introduction, $G_0 = 2e^2/h$ is the quantum of conductance, and T is the total transmission.

To investigate the influence of a small bias voltage, we have computed for Ag and Pt the transmission $T(E)$ in an energy interval of width $2\Delta = 100$ meV around the Fermi energy.[51] The averaged conductance

$$\langle G\rangle = G_0\langle T\rangle = G_0\frac{1}{2\Delta}\int_{E_F-\Delta}^{E_F+\Delta} T(E)\,dE, \quad (11)$$

can then be compared to the conductance $G = G_0 T(E_F)$ at the Fermi energy (cf. Eq. (10)). This provides information on the nonlinearity of current-voltage characteristics, although the formulas we use are, strictly speaking, only valid for the zero-bias situation.

C. Local density of states calculations

To gain some insight into the electronic states relevant for the transport through our nanowires, we shall also compute the local density of states (LDOS) projected onto particular atoms. The computation of the LDOS requires the evaluation of the Green function of the central part of the nanowire $\hat{G}_{CC,\sigma}$ (cf. Eq. (4)). From $\hat{G}_{CC,\sigma}$ we construct the LDOS via a Löwdin transformation.[52] The LDOS for a particular orbital α of atom i is then given by[53]

$$\mathrm{LDOS}_{i\alpha,\sigma}(E) = -\frac{1}{\pi}\mathrm{Im}\left[\hat{S}^{1/2}_{CC}\hat{G}^r_{CC,\sigma}(E)\,\hat{S}^{1/2}_{CC}\right]_{i\alpha,i\alpha}. \quad (12)$$

In the case of the nonferromagnetic metals (Ag and Pt) the LDOS will in the following be given only for one spin component, because of the spin degeneracy.

III. SILVER ATOMIC CONTACTS

We start the analysis of our results with the discussion of the conductance of Ag nanowires. Ag is, like Au, a noble metal with a single valence electron. Different experiments have shown that the conductance of Ag contacts exhibits a tendency towards quantized values in the last stages of the wire formation.[54,55,56] In fact, the most dominant feature in the experimental low-temperature conductance histogram is a pronounced peak at $1\,G_0$.[54,55]

A. Evolution of individual silver contacts

Let us first describe some typical examples of the breaking of Ag nanowires. In Fig. 1 we show the formation of a single-atom contact. Beside the strain force we display the conductance G, the averaged conductance $\langle G\rangle$ (cf. Eq. (11)), the MCS radius and the channel transmissions. As one can see, after an initial evolution up to an elongation of 0.2 nm (region with eight conduction channels), which is similar for all the 50 Ag contacts studied, the conductance starts decreasing in a step-like manner which changes from realization to realization. The

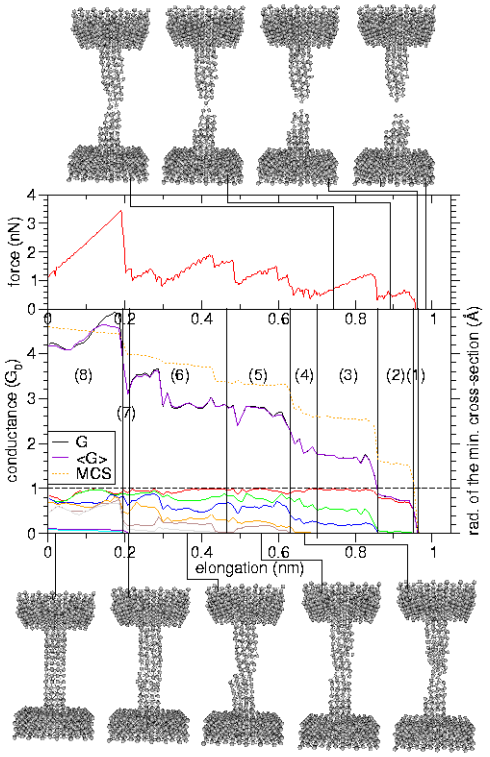

Figure 1: (Color online) Formation of a single-atom contact for Ag (4.2 K, [001] direction). The upper panel shows the strain force as a function of the elongation of the contact. In the lower panel the conductance G, the averaged conductance $\langle G \rangle$, the MCS (minimum cross-section) radius and the channel transmissions are displayed. Vertical lines separate regions with different numbers of open channels ranging from 8 to 1.[57] Above and below these graphs snapshots of the stretching process are shown.

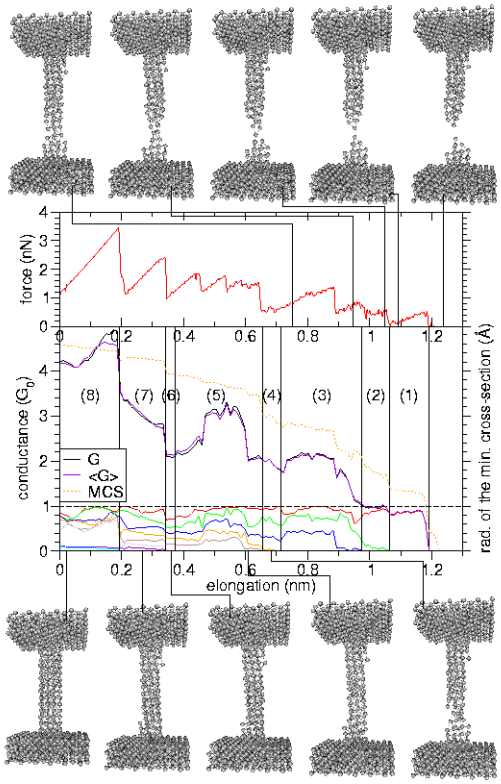

Figure 2: (Color online) Formation of a dimer configuration for Ag (4.2 K, [001] direction). The upper panel shows the strain force as a function of the elongation of the contact. In the lower panel the conductance G, the averaged conductance $\langle G \rangle$, the MCS (minimum cross-section) radius and the channel transmissions are displayed. Vertical lines separate regions with different numbers of open channels ranging from 8 to 1.[57] Above and below these graphs snapshots of the stretching process are shown.

jumps in the conductance usually occur at plastic deformations of the contact, i.e. when bonds break and sudden atomic rearrangements take place. Such sudden rearrangements are visible as a break-in of the strain force. The elastic stages, in which the atomic bonds are being stretched, are characterized by a linear increase of the strain force. In this case the conductance exhibits well-defined plateaus (see for instance the region with three channels, which occurs for elongations between 0.7 nm and 0.83 nm). In the last stages of the breaking of the contact, displayed in Fig. 1, a stable single-atom contact is formed. In this region the conductance is mainly dominated by a single channel, although a second one is still visible (see two-channel region or elongations between 0.86 nm and 0.95 nm). Subsequently, a dimer structure is formed, which survives for a short period of time, after which the contact finally breaks. In this region only a single transmission channel is observed.

It is worth noticing that there is practically no difference between the conductance G and the averaged conductance $\langle G \rangle$ (cf. Eq. (11)), demonstrating that the transmission as a function of the energy is rather flat around the Fermi energy (in the window $-\Delta \leq E - E_F \leq \Delta$). This can be seen explicitly in Fig. 3, which we shall discuss later in more detail. The flat transmission $T(E)$ is expected for a noble metal like Ag because its density of states around E_F is mainly dominated by the contributions of the s and p bands, which are rather broad and vary slowly with energy.

Another example of a breaking curve for Ag is depicted in Fig. 2. In the beginning the conductance evolves like for the contact discussed above (cf. Fig. 1). This time a stable dimer is finally formed. Prior to the formation of the dimer structure, which sustains a single channel (see one-channel region or elongations from 1.06 nm to 1.19 nm), there also appears a single-atom contact, where two channels are still visible (see two-channel region or elongations from 0.97 nm to 1.06 nm), in analogy to what has been found for Au before.[37] We observe for both configurations a single dominant transmission channel and a conductance of around $1\,G_0$. This result is consistent

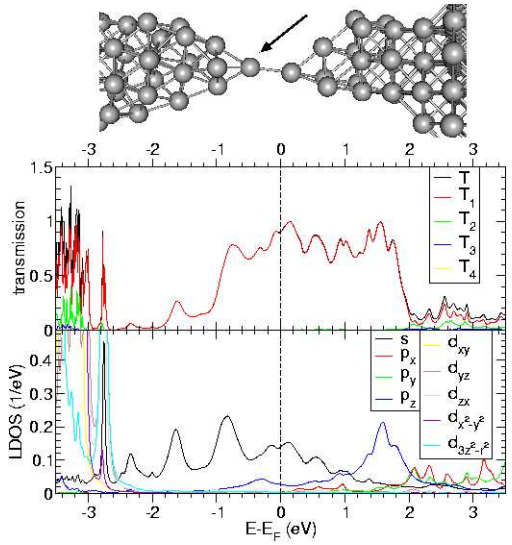

Figure 3: (Color online) Ag contact of Fig. 2 at an elongation of 1.16 nm. The total transmission T is plotted as a function of the energy together with the contributions from the different transmission channels T_n. Additionally the LDOS (local density of states) is given for an atom in the narrowest part of the contact, where the different orbital contributions have been itemized. Above the figure the narrowest part of the Ag contact is displayed in a magnified fashion and the atom is indicated, for which the LDOS is shown.

with first-principles calculations, where it has been shown for selected ideal contact geometries that the transmission of Ag chains is around $1\,G_0$ and the conductance is carried by a single transmission channel.[58,59]

Due to the appearance of a stable dimer structure there is now a long and flat last plateau before rupture in Fig. 2. Our simulations show that this type of dimer is the most common structure in the last stages of the contact formation.

A certain peculiarity can be observed, if one has a closer look at the region with six open channels. Here, the conductance first drops abruptly and then it increases again in the region with five open channels. Notice that this increase is accompanied by a steady decrease of the MCS. This type of reentrance of the conductance, which is often observed experimentally, cannot be explained in terms of semiclassical arguments, which are based on Eq. (1). According to this formula the conductance should be a monotonous function of the MCS, which, however, is not always the case. Such break-ins of the conductance have already been observed before in simpler TB calculations.[27]

In order to explain the existence of a single channel in the final stages of breaking, we have plotted in Fig. 3 the LDOS of an atom in the narrowest part of the junction as a function of the energy together with the transmission. We have chosen a dimer configuration at an elongation of 1.16 nm, right before the rupture of the contact displayed in Fig. 2. The transmission around the Fermi energy is made up of a single channel, exhibiting only a tiny variation in the energy window $-\Delta \leq E - E_F \leq \Delta$. In the LDOS there are two dominant contributions, one coming from the s orbital, as expected, and the other one from the p_z orbital. Therefore, the transmission channel is expected to consist mainly of these two contributions, the other orbitals being of minor importance. As found before,[8,50] the s and p_z orbitals are then forming a radially isotropic transmission channel along the transport direction. If we denote by l_z the projection of the angular momentum onto the z axis (transport direction), this channel has the quantum number $l_z = 0$.

B. Statistical analysis of silver contacts

In Fig. 4 our computed MCS histogram as well as the computed conductance histogram are displayed. The histograms are obtained by collecting the results of the stretching of 50 Ag contacts oriented along the [001] direction at 4.2 K, as described in Sec. II. In the case of the MCS histogram, the most remarkable feature is the appearance of very pronounced peaks, which indicate the existence of particularly stable contact radii. For the purpose of correlating these peaks with the structure in the conductance histogram, we have marked the regions around the peaks in the MCS histogram with different pattern styles. In the conductance histogram we indicate the counts for conductances belonging to a certain MCS region with the same pattern style, in order to establish this correlation between the geometric structure of the contacts and the features in the conductance histogram.

With respect to the conductance histogram, our main result is the appearance of a pronounced peak at $1\,G_0$, in accordance with the experimental results.[54,55,56] This peak mainly stems from the contributions of contacts with MCS radii in the first (dimers) and second (single-atom contacts) region of the MCS histogram. Therefore, we can conclude that the peak at $1\,G_0$ is a consequence or manifestation of the formation of single-atom contacts and dimers in the last stages of the breaking of the Ag wires.

It is also important to stress that the contributions to the conductance histogram coming from different regions of the MCS histogram clearly overlap. This means in practice that the MCS radius is not the only ingredient that determines the conductance, as one would conclude from semiclassical arguments (see Eq. (1)). In other words, the peak structure in the MCS histogram is not simply translated into a peak structure in the low-temperature conductance histogram, as suggested in Ref. 23.

At this stage, a word of caution is pertinent. In break junction experiments, contacts are opened and closed repeatedly, and the breaking processes starts with a conductance as large as $100\,G_0$.[17] Compared to this value, our simulations start with a very small conductance of around $4\,G_0$. Additionally, all the contacts are oriented

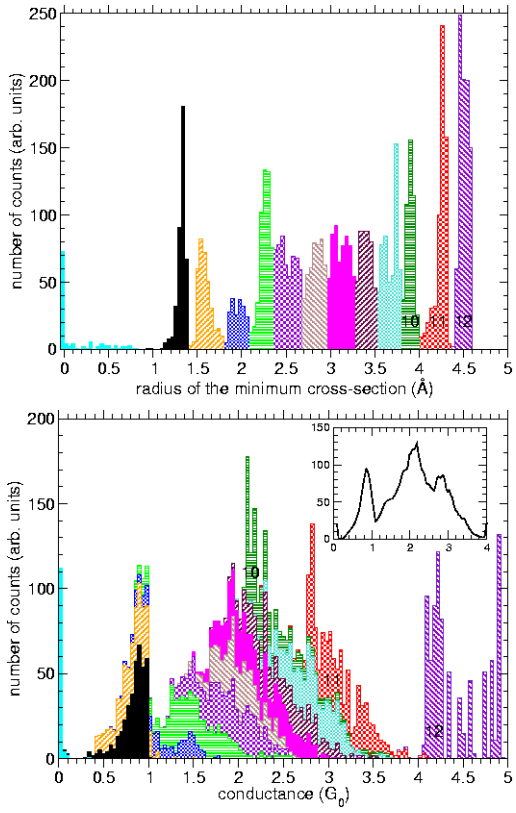

Figure 4: (Color online) MCS (minimum cross-section) histogram (upper panel) and conductance histogram (lower panel) for Ag (4.2 K, [001] direction, 50 contacts). In the MCS histogram different regions of frequently occurring radii have been defined with different pattern styles. The patterns in the conductance histogram indicate the number of counts for conductances belonging to the corresponding region of the MCS histogram. For better reference in the text, some regions in the MCS and conductance histogram have additionally been labeled with numbers. In the inset of the lower panel the conductance histogram is displayed in the relevant region in a smoothed version by averaging over six nearest-neighbor points.

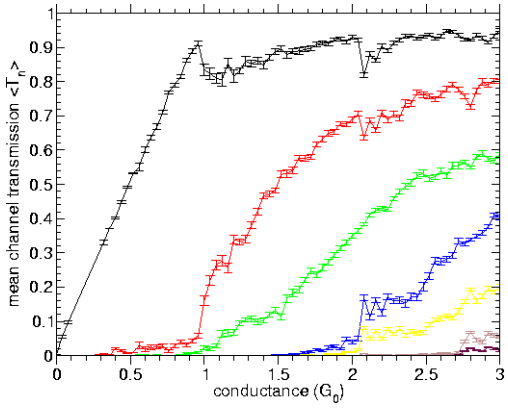

Figure 5: (Color online) Mean value of the transmission coefficient $\langle T_n \rangle$ as a function of the conductance for Ag (4.2 K, [001] direction, 50 contacts). The error bars indicate the mean error.[61]

along the [001] direction, which can be expected to have an influence on the structure of the conductance histogram. Even for rather thick contacts it has been shown experimentally that prefabricated wires cause a different peak structure in the conductance histograms.[60]

The last three peaks of the MCS histogram (labeled 10, 11 and 12 in Fig. 4) are mainly dominated by the (arbitrarily) selected [001] starting-configuration. It is interesting to observe that the MCS region labeled with a 10 has a large weight at conductances of somewhat above $2\,G_0$, although it should be expected to have contributions for large transmissions because of its high MCS. The break-in of the conductance in Fig. 2 at the transition from the six- to five-channel region is an example showing the origin of the large weight of this MCS region at $2\,G_0$. This observation illustrates that even conductance regions down to $2\,G_0$ are distorted due to the small size of our contacts. While we can be sure about the first peak in the conductance histogram at $1\,G_0$, all the higher peaks would require the study of bigger contacts with even more atoms in the central region.

It is important to remark that out of 50 simulations we have only observed the formation of three short chains with 3, 4 and 5 atoms in each case. This is in strong contrast to the case of Au, where chains were encountered much more frequently and with more chain atoms.[37] Short atomic Ag chains of up to three atoms have also been observed in experiments.[55,56]

Another important piece of information can be obtained from the analysis of the mean channel transmission (averaged over all contacts) as a function of the conductance, which is shown in Fig. 5.[61] Here, one can see that the conductance region below $1\,G_0$ is largely dominated by a single channel. Above $1\,G_0$ a sharp onset of the second transmission channel can be observed, the third channel increasing more continuously. At $2\,G_0$ again an onset of the fourth and fifth channel are visible.

These results can be related to the experimental observation on noble metals made by Ludoph *et al.*,[54,62] namely the principle of the "saturation of channel transmission". This principle says that there is "a strong tendency for the channels contributing to the conductance of atomic-size Au contacts to be fully transmitting, with the exception of one, which carries the remaining fractional conductance".[62] This tendency of the channels to open one by one is evident for the first channel from Fig. 5 and also experimentally the first peak in the conductance histogram for Ag fulfills this principle best.[54] Concerning the higher conductances the finite size of our contacts plays an increasingly restrictive role, but we are well in line with the statement (made for Au, Ag and Cu) that "particularly the second peaks in the histograms are also determined by other statistical (probably atomic) properties of the contact".[54]

IV. PLATINUM ATOMIC CONTACTS

Now, we turn to the analysis of Pt contacts. Pt is a transition metal with 10 valence electrons in the partially occupied $5d$ and $6s$ orbitals. The experiments reported so far show that in the case of Pt the last conductance plateau lies typically above $1\,G_0$. Consequently, the conductance histogram is dominated by the presence of a broad peak centered around $1.5\,G_0$.[55,63] Another remarkable feature of Pt contacts is the appearance of monoatomic chains (with up to six atoms), which have a conductance ranging from around 1.5 to $1.0\,G_0$ as the length increases.[64,65] Moreover, complex oscillations of the conductance as a function of the number of chain atoms are superimposed on top of such a decay. Their origin has been explained in terms of a nearly half-filled s band and the additional conduction channels provided by the almost full d bands.[66]

A. Evolution of individual platinum contacts

In Fig. 6 a typical example of the formation of a dimer configuration is shown. As before, beside the strain force, we display the conductance, the averaged conductance, the MCS radius and the channel transmissions. The initial evolution is quite similar for all the 50 Pt contacts analyzed here. In this region, which corresponds to elongations below 0.17 nm, we observe between 11 and 10 open conduction channels. After this region, and as in the case of Ag contacts, the conductance evolves in a series of jumps which coincide with plastic deformations (see the positions of break-ins in the sawtooth shape of the strain force). However, in contrast to Ag, now we find strong conductance fluctuations during the different elastic plateaus. The stretching of the contact of Fig. 6 ends with the formation of a dimer, which sustains three open channels and has a conductance above $1\,G_0$ (see region with elongations between 1.12 nm and 1.22 nm). This is again contrary to the Ag junctions discussed above, where only a single dominant channel is observed in the final stages before rupture.

On the other hand, the comparison between the conductance G and the averaged conductance $\langle G\rangle$ shows certain deviations (see for instance the region with four channels). This fact indicates that for Pt there is a much stronger variation of the transmission as a function of the energy around the Fermi energy, as compared with Ag. This is in agreement with the experimental finding of nonlinear current-voltage characteristics for Pt as opposed to linear ones for a noble metal like Au.[67]

The clear differences between the Pt and the Ag contacts can be traced back to the difference in their electronic structure, as we now proceed to illustrate. We show in Fig. 7 the LDOS for an atom in the narrowest part of the junction as a function of the energy together with the transmission. We have chosen a dimer configuration at an elongation of 1.18 nm just before the rupture

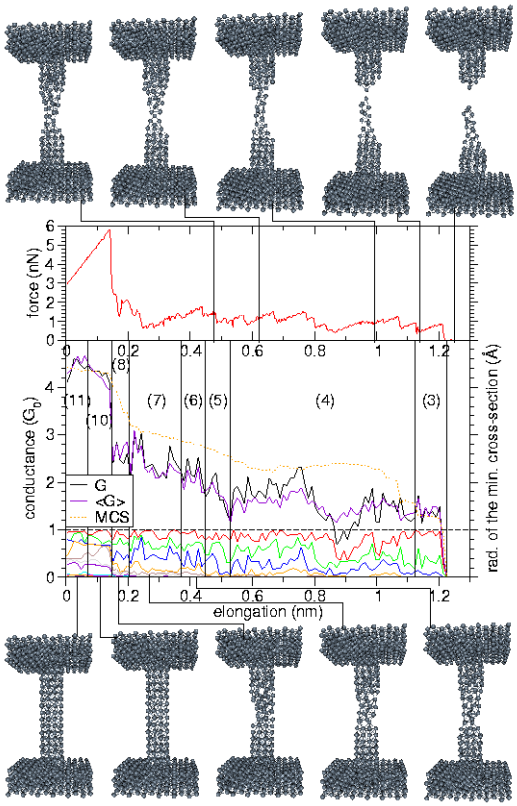

Figure 6: (Color online) Formation of a dimer configuration for Pt (4.2 K, [001] direction). The upper panel shows the strain force as a function of the elongation of the contact. In the lower panel the conductance G, the averaged conductance $\langle G\rangle$, the MCS (minimum cross-section) radius and the channel transmissions are displayed. Vertical lines separate regions with different numbers of open channels ranging from 11 to 3.[57] Above and below these graphs snapshots of the stretching process are shown.

of the contact of Fig. 6. Notice the presence of a much more pronounced structure in the transmission around the Fermi energy as compared to Fig. 3, which can be attributed to the contribution of d states. This fact naturally explains the deviation between the conductance G at E_F and the averaged conductance $\langle G\rangle$ (cf. Fig. 6). At the same time, the partially occupied d orbitals are also responsible for the larger number of open transmission channels (three in the dimer region of Fig. 6), as they provide additional paths for electron transfer between the two electrodes.

From Fig. 7 it is evident that d states play a major role for the conductance in Pt contacts. The strong fluctuations of the conductance during the elastic stages of stretching, as observed in Fig. 6, point out a high sensitivity of these d states to the atomic configurations. These two phenomena, namely the pronounced structure of the transmission around the Fermi energy and the sensitivity of d states to atomic configurations are related.

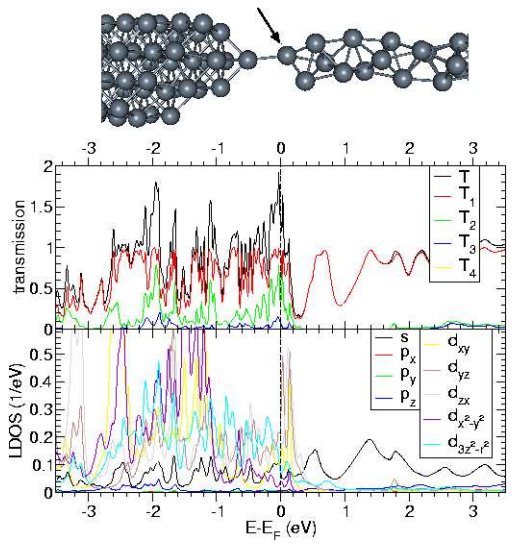

Figure 7: (Color online) Pt contact of Fig. 6 at an elongation of 1.18 nm. The total transmission T is plotted as a function of the energy together with the contributions from the different transmission channels T_n. Additionally the LDOS (local density of states) is given for an atom in the narrowest part of the contact, where the different orbital contributions have been itemized. Above the figure the narrowest part of the Pt contact is displayed in a magnified fashion and the atom is indicated, for which the LDOS is shown.

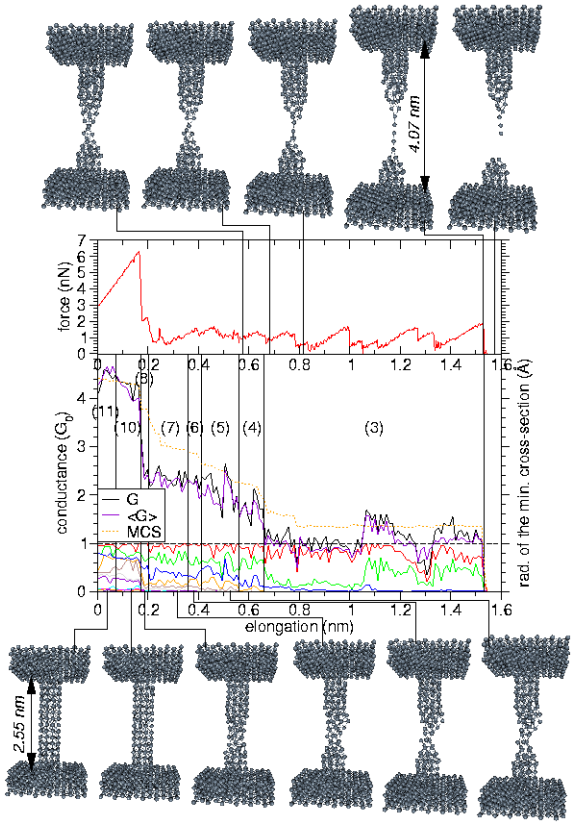

Figure 8: (Color online) Formation of a five-atom chain for Pt (4.2 K, [001] direction). The upper panel shows the strain force as a function of the elongation of the contact. In the lower panel the conductance G, the averaged conductance $\langle G \rangle$, the MCS (minimum cross-section) radius and the channel transmissions are displayed. Vertical lines separate regions with different numbers of open channels ranging from 11 to 3.[57] Above and below these graphs snapshots of the stretching process are shown.

Indeed, a slight variation of E_F for a fixed contact geometry has a similar effect on the conductance as the modification of electronic level positions caused by a variable contact geometry but a fixed Fermi energy. Ultimately, the sensitivity of d states to atomic configurations can be attributed to the spatial anisotropy of the d orbitals as compared to the spatially isotropic s orbitals, which are responsible for the conductance in Ag contacts.

Now we proceed to discuss the formation of chains in Pt contacts. In the last stages of our simulations we often observe the formation of special structures, namely linear chains of several atoms. In Fig. 8 we show the evolution of a Pt contact, which features a five-atom chain before rupture. As for the contact discussed previously, substantial fluctuations in the conductance are visible even during the elastic stages, demonstrating again the sensitivity of d orbitals to atomic positions. The conductance during the formation of the chain is mainly dominated by two channels, but also a third one is contributing slightly. The first two channels can be of nearly the same magnitude (see elongations above 1.1 nm). After the dimer has formed, the transmission fluctuates around $1\,G_0$. Compared with Ag, the conductance can, however, also be higher than $1\,G_0$ due to the presence of a second and a third open channel. The conductance of the last plateau is slightly below the typical experimental value of $1.5\,G_0$,[55,68] a fact that we shall discuss below.

During the formation of the chain (see three-channel region or elongations above 0.8 nm), the strain force exhibits a clear sawtooth behavior. The abrupt jumps in the force after the long elastic stages signal the incorporation of a new atom into the chain. Such incorporations happen at elongations of 0.79 nm (dimer), 1.00 nm (three-atom chain), 1.05 nm (four-atom chain) and 1.27 nm (five-atom chain). Additional jumps at 0.83 nm, 1.11 nm and 1.33 nm are due to bond breakings at the chain ends. Note that the incorporation of a new atom into an atomic chain does not always require long stretching distances of the order of the nearest-neighbor distance. Because of metastabilities depending on the geometry of the junction, they may actually be much shorter, as can be inferred from the transition from the three-atom chain to the four-atom chain.

In order to explore changes in the electronic structure and their influence on the transmission for the evolution from a dimer and to long atomic chain, we analyze these two kinds of structures now in more detail. In Fig. 9 we plot the transmission and LDOS as a function of the energy, considering as example the contact of Fig. 8. As

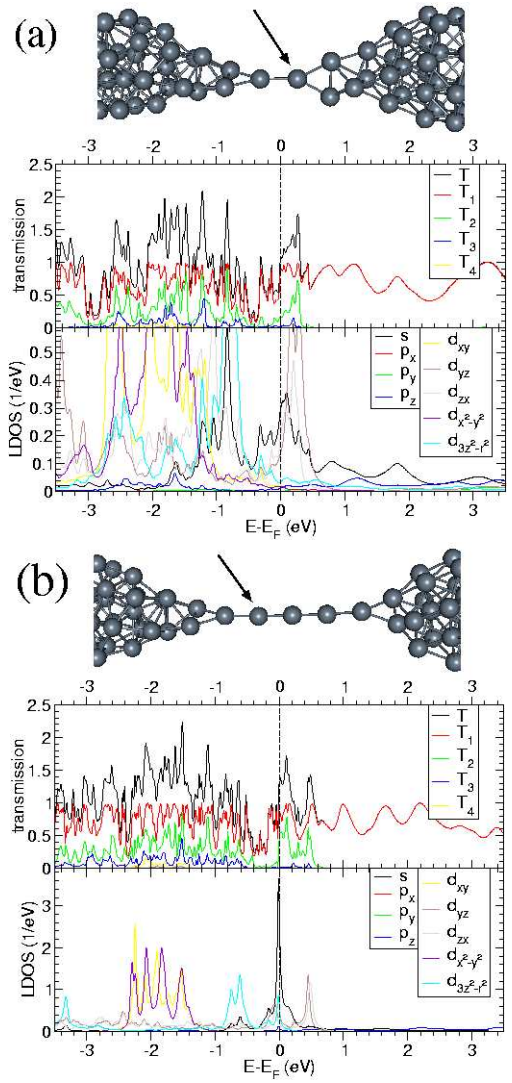

Figure 9: (Color online) Pt contact of Fig. 8 at an elongation of 0.95 nm, when the contact is forming a dimer (a) and at an elongation of 1.44 nm, when the contact is forming a five-atom chain (b). In each case the total transmission T is plotted as a function of the energy together with the contributions from the different transmission channels T_n. Additionally the LDOS (local density of states) is given for an atom in the narrowest part of the contact, where the different orbital contributions have been itemized. Above each figure the narrowest part of the Pt contact is displayed in a magnified fashion and the atom is indicated, for which the LDOS is shown.

can be seen in Fig. 9(a) for the case of the dimer, the main contributions to the LDOS at the Fermi energy come from the s, d_{yz}, d_{zx} and $d_{3r^2-z^2}$ orbitals. Just like for the dimer structure investigated above, the d orbitals contribute significantly to the LDOS (cf. Fig. 7). While the energy dependence of the transmission looks qualitatively similar, the LDOS changes dramatically when a long chain is formed (see Fig. 9(b)). We observe a pinning of the s and $d_{3r^2-z^2}$ states at the Fermi energy, where the s state is close to half filling corresponding to an electronic $5d^9 6s^1$ configuration of the Pt atom. (Notice also the change in scale for the LDOS when going from Fig. 9(a) to Fig. 9(b).) Comparing the energy dependence of the transmission channels and the LDOS in Fig. 9(b), we can infer that the first channel is a linear combination of s, p_z and $d_{3r^2-z^2}$ orbitals ($l_z = 0$), while the second and third seem dominated by d_{yz} and d_{zx} orbital contributions ($l_z = \pm 1$). These findings are perfectly in line with Ref. 66.

It is also noteworthy that when the d states have decayed 1 eV above the Fermi energy and the s contribution dominates in the LDOS, only a single channel is observed in the transmission for both the dimer and the chain configuration (see Figs. 7 and 9). This would correspond exactly to the situation described above for Ag wires, and demonstrates that the differences between these two metallic contacts (Ag and Pt) are mainly due to the different positions of their Fermi energy.

B. Statistical analysis of platinum contacts

Putting together all the results for the 50 Pt contacts simulated in our study, we obtain the histograms for the MCS and conductance shown in Fig. 10. The MCS histogram exhibits a very pronounced peak at radii corresponding to dimer contacts and chains of atoms. Out of 50 breaking events we obtain 18 chains, 17 chains ranging from 5 to 11 atoms and one with up to 19 atoms. The tendency of Pt to form atomic chains is consistent with experiments,[55,64] but the ratio of chain formation is obviously higher than in the experiments. This could partly be due to the thinness of the contacts that we investigate. There exists experimental evidence for the formation of chains with lengths up to six atoms,[55] while longer chains become more and more unlikely. Therefore, our chains with more than eight atoms seem somewhat artificial.

In the conductance histogram the low-lying MCS peak for dimers and atomic chains gives rise to a very broad peak in the conductance histogram. The position of this peak is centered around $1\,G_0$ rather than $1.5\,G_0$, as in the experiment.[55,68] If we exclude the longest chains (chains with more than eight atoms), we obtain a conductance histogram with a very broad peak at $1.15\,G_0$ (cf. inset in Fig. 10).

Experimentally it has been shown that the peak at $1.5\,G_0$ shifts to $1.8\,G_0$ for higher bias voltages.[68] This has been attributed to a structural transition, where atomic chains are replaced by single-atom contacts. Thus, the conductance of dimers and chains should be around $1.5\,G_0$ and the conductance of single-atom contacts around $1.8\,G_0$. In Fig. 2 of Ref. 65 Smit *et al.* reported a decrease of the average conductance from $1.5\,G_0$ to around $1\,G_0$ for increasing chain lengths. This demonstrates that our broad distribution of conductances around $1\,G_0$ in the conductance histogram (cf. Fig. 10) is not unreasonable, although the transmis-

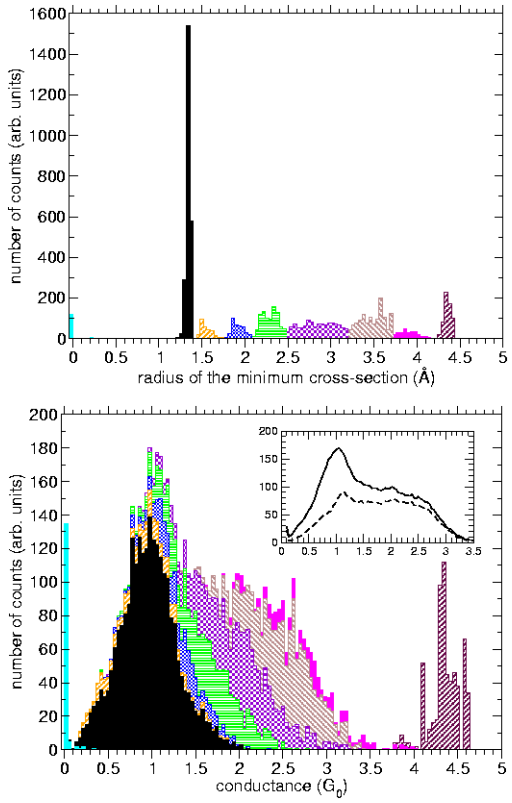

Figure 10: (Color online) MCS (minimum cross-section) histogram (upper panel) and conductance histogram (lower panel) for Pt (4.2 K, [001] direction, 50 contacts). In the MCS histogram different regions of frequently occurring radii have been defined with different pattern styles. The patterns in the conductance histogram indicate the number of counts for conductances belonging to the corresponding region of the MCS histogram. In the inset of the lower panel the conductance histogram is displayed in the relevant region in a smoothed version by averaging over six nearest-neighbor points for all contacts (solid) and contacts with up to 8 atoms in the chain (dotted).

sion for dimers and short chains seems to be underestimated. A recent DFT study investigated ideal Pt chains consisting of two to five atoms in the [001] direction.[69] Conductances between $2\,G_0$ and $1\,G_0$ were obtained with a trend toward $1\,G_0$ for longer chains in agreement with experiment. The structure of the chains, which in our case is linear, was zigzag-like. This could be another explanation for the lower transmissions in our study.[70]

Although the peak position in the conductance histogram in Fig. 10 is lower than in the experiments, we want to point out the strong qualitative differences in comparison to Ag. While the first two MCS peaks in the Ag histogram (cf. Fig. 4) are restricted to conductance values below $1\,G_0$, this is not the case for Pt. Here, the first two peaks cover a range of conductance values from as low as $0.1\,G_0$ up to $2\,G_0$. This is again due to the contribution of the d orbitals at the Fermi energy, which leads to a higher number of open channels in the case of

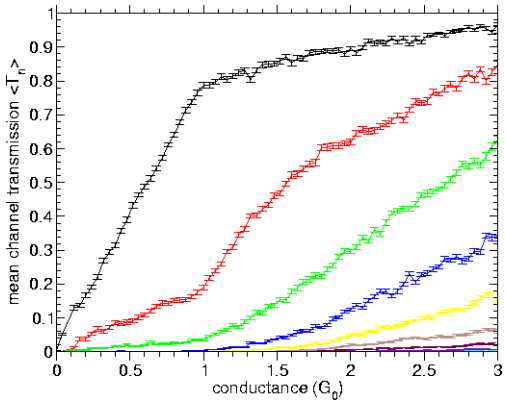

Figure 11: (Color online) Mean value of the transmission coefficient $\langle T_n \rangle$ as a function of the conductance for Pt (4.2 K, [001] direction, 50 contacts). The error bars indicate the mean error.[61]

Pt, as explained in Sec. IV A. Let us recall that for Ag there is a single dominant transmission channel (and a small second one), while for Pt there are usually three channels in the last stages of breaking, and the second channel can be comparable in magnitude to the first. As explained above, the extraordinary width of the first peak in the conductance histogram for Pt can be attributed to the sensitivity of d states to the atomic configuration of the contact.

This qualitative difference in the number of conduction channels is illustrated in Fig. 11, where we show the mean value of the transmission coefficients as a function of the conductance.[61] Notice that as compared with the case of Ag (cf. Fig. 5), there are contributions from the second and third channel already present for conductances below $1\,G_0$. For conductances of $1.5\,G_0$ there are four or five channels on average.

In conclusion, the different behavior of Ag and Pt contacts stems from the different electronic states present at the Fermi energy. While for noble metals like Au and Ag it is located in the s band, its position is shifted downwards into the d bands for Pt. Therefore, in the latter case there are in general more open channels contributing to the conductance. This confirms the statements of Scheer *et al.*[7] that the number of transmission channels is determined by the chemical valence.

V. ALUMINUM ATOMIC CONTACTS

Al is an example of the so-called *sp*-like metals. In the crystalline form there are three valence electrons occupying partly the $3s$ and $3p$ bands around the Fermi energy. In this respect, Al has a very different electronic structure as compared to Au, Ag or Pt, and in this section we study how this electronic structure is reflected in the conductance through Al atomic wires. Due to the technical problems detailed below, this analysis will be considerably shorter than for the other metals.

The experimental studies of the conductance of Al atomic-sized contacts have shown several peculiar features.[5,8,55,71,72] For instance, Scheer *et al.*[5], making use of the superconducting current-voltage characteristics to extract the transmission coefficients, showed that usually three conduction channels contribute to the transport, although the conductance of the last plateau is typically below $1\,G_0$. This was explained in Ref. 6 in terms of the contribution of the p orbitals to the transport. Exploiting conductance fluctuations, the presence of several conduction channels for conductances above $0.5\,G_0$ could subsequently be confirmed by another independent experimental technique.[54] As an additional peculiarity, Al is one of the few multivalent metals which exhibits several pronounced peaks in the conductance histograms at low temperatures.[72] The first peak appears at around $0.8\,G_0$ and the next ones at $1.9\,G_0$, $3.2\,G_0$ and $4.5\,G_0$. Furthermore, the conductance plateaus in Al have a positive slope upon stretching,[5,71] which is quite unique.

Again we simulated 50 breaking events. Although we always observe in the last stage of the nanocontacts either a single-atom contact (36 times), a dimer (13 times) and in one case a four-atom chain, the single-atom contacts and dimers are often very short-lived configurations and less stable than the corresponding Ag and Pt structures. We attribute this to shortcomings in the semiempirical potential employed for Al in this work. Previously it has been shown that this potential cannot reproduce adequately the mechanical properties of an infinite Al chain.[73] This underestimation of the stability of thin wires is quite apparent in our simulations, where the contacts break effectively at conductances well above $1.5\,G_0$ and with several atoms present in the MCS.

This technical problem hindered the proper analysis of the statistical properties of Al contacts. However, we could recover a few sensible examples. One of the formations of a relatively stable dimer is displayed in Fig. 12. A region of three transmitting channels can be observed shortly before contact rupture, and the conductance of the dimer configuration is close to $1\,G_0$, which agrees nicely with the observations of Scheer *et al.*[5] The origin of these three channels is, as explained in Ref. 6, the contribution of the partly occupied *sp*-hybridized valence orbitals of Al to the transport. Before this region, a nice plateau around $2\,G_0$ is visible. Both features agree well with the peaks in the experimental conductance histogram for Al close to $0.8\,G_0$ and $1.9\,G_0$.[55,72] More importantly, our results reproduce the peculiar positive slopes of the last plateaus of the stretching curves, in compliance with Refs. 5,8,34,71.

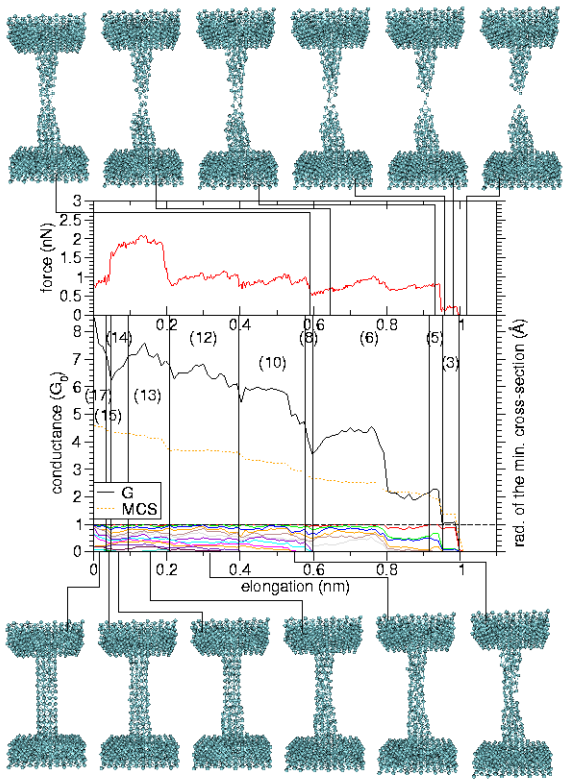

Figure 12: (Color online) Formation of a dimer configuration for Al (4.2 K, [001] direction). The upper panel shows the strain force as a function of the elongation of the contact. In the lower panel the conductance G, the MCS (minimum cross-section) radius and the channel transmissions are displayed. Vertical lines separate regions with different numbers of open channels ranging from 17 to 3.[57] Above and below these graphs snapshots of the stretching process are shown.

VI. NICKEL ATOMIC CONTACTS

During the last years a lot of attention has been devoted to the analysis of contacts of magnetic materials.[74,75,76,77,78,79,80] (For a more complete list of references see Refs. 1,80.) In these nanowires the spin degeneracy is lifted, which can potentially lead to interesting spin-related phenomena in the transport properties. For instance, different groups have reported the observation of half-integer conductance quantization either induced by a small magnetic field[76] or even in the absence of a field.[78,79] These observations are quite striking since such quantization requires simultaneously the existence of a fully spin-polarized current and perfectly open conduction channels.[81] With our present understanding of the conduction in these metallic junctions, it is hard to believe that these criteria can be met, in particular, in the ferromagnetic transition metals (Ni, Co and Fe). As a matter of fact, in a more recent study by Untiedt *et al.*,[80] carried out at low temperatures and under cryogenic vacuum conditions, the complete absence of quantization in atomic contacts of Ni, Co and Fe has been reported, even in the presence of a magnetic field as high as 5 T. Several recent model calculations support these findings.[82,83,84,85]

In this section we address the issue of the conductance

quantization and the spin polarization of the current with a thorough analysis of Ni contacts. As described in Sec. II B we apply our method to a Hamiltonian with spin-dependent matrix elements.[46]

A. Evolution of individual nickel contacts

In Fig. 13 we show the evolution of the conductance during the formation of a Ni dimer structure, which is the most common geometry in the last stages of the breaking process. Beside the evolution of the conductance and transmission eigenchannels for both spin components separately, we have plotted the MCS radius, strain force, spin polarization of the current and contact configurations. The spin polarization P, shown in the inset of the lower panel, is defined as

$$P = \frac{G^{\uparrow} - G^{\downarrow}}{G^{\uparrow} + G^{\downarrow}} \cdot 100\%, \tag{13}$$

where G^{σ} is the conductance of the spin component σ (cf. Eq. (8)). Here, spin up ($\sigma = \uparrow$) means majority spins and spin down ($\sigma = \downarrow$) minority spins. Notice that in the last stages of the stretching the conductance is dominated by a single channel for the majority spins, while for the minority spin there are still up to four open channels. In the final stages (see regions with three or one open channel(s) for $G^{\uparrow}$) the conductance for the majority spin lies below $1.2e^2/h$, while for the minority spin it is close to $2e^2/h$, adding up to a conductance of around 1.2-1.6 G_0.

With respect to the evolution of the spin polarization of the current, in the beginning of the stretching process it takes a value of around -40%, i.e. the conductance of the minority-spin component outweighs that of the majority-spin component. This is expected from the bulk density of states of Ni. For this transition metal the Fermi level lies in the s band (close to the edge of the d bands) for the majority spins and in the d bands for the minority spins. For this reason, there is a larger number of conduction channels for minority-spin component. This value of P is indeed quite close to the value of the spin polarization of the bulk density of states at the Fermi energy, which in our model is equal to -40.5%. As the contact geometry starts changing, the spin polarization of the current begins to fluctuate. It increases even to values of above 0%, but keeps a tendency towards negative values, until it starts increasing to over $+80\%$ in the tunneling regime, when the contact is broken.

Let us now try to gain further insight into these findings. We show in Fig. 14 the transmission as a function of the energy together with the LDOS for an atom in the narrowest part of the constriction portrayed in the upper part of the figure. It can be observed that the Fermi energy, as in bulk, is located just at the edge of the d states for the majority-spin component, while it is inside the d states for the minority-spin component. The majority-spin component therefore exhibits a single transmission channel, behaving like a noble metal (cf. results for Ag in Sec. III), while there are several open channels for the minority-spin component like in the case of a transition metal (cf. results for Pt in Sec. IV).

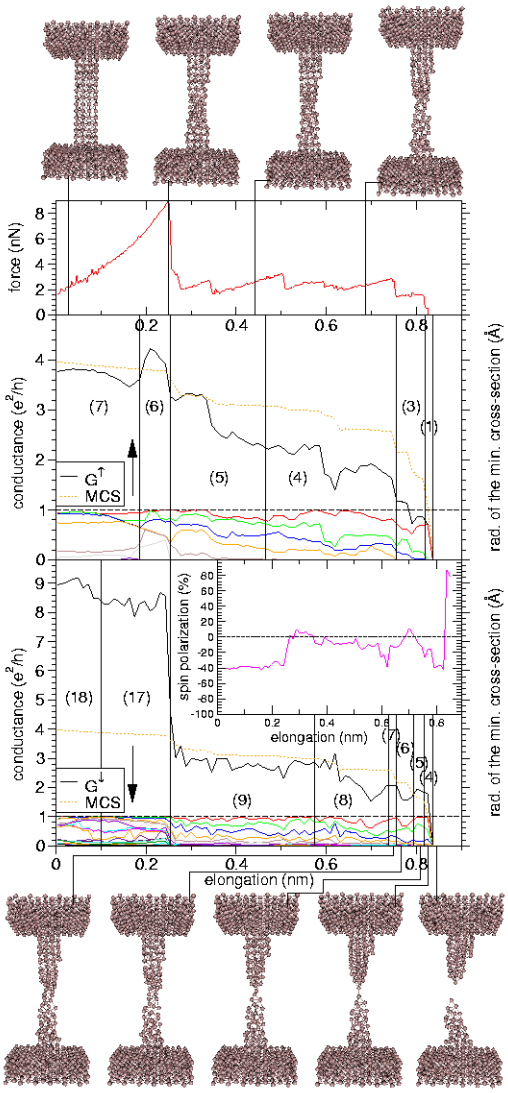

Figure 13: (Color online) Formation of a dimer configuration for Ni (4.2 K, [001] direction). The upper panel shows the strain force as a function of the elongation of the contact. In the lower two panels the conductance G^{σ}, the MCS (minimum cross-section) radius and the channel transmissions are displayed for the respective spin component σ. Vertical lines separate regions with different numbers of open channels ranging from 7 to 1 and 18 to 4, respectively.[57] An inset shows the evolution of the spin polarization. Above and below these graphs snapshots of the stretching process are shown.

Concerning the spin polarization of the current, the large density of states at E_F for the minority-spin component usually gives rise to a higher number of open channels for the minority-spin component than for the majority-spin component, which in turn leads to a negative spin polarization of the current. However, this ar-

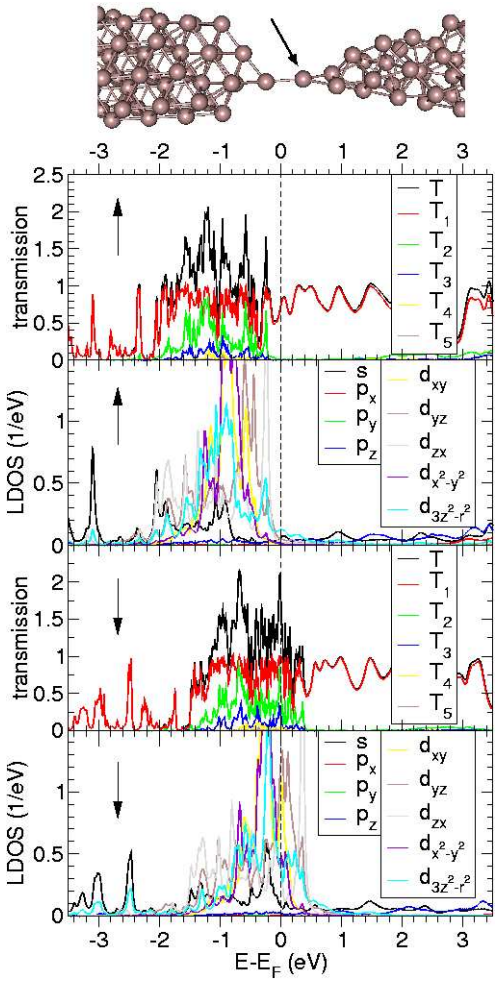

Figure 14: (Color online) Ni contact of Fig. 13 at an elongation of 0.83 nm. The transmission is plotted as a function of the energy together with the contributions from the different transmission channels T_n^σ for the respective spin component σ. Additionally the LDOS (local density of states) is given for each spin component for an atom in the narrowest part of the contact, where the different orbital contributions have been itemized. Above the figure the narrowest part of the Ni contact is displayed in a magnified fashion and the atom is indicated, for which the LDOS is shown.

gument is just qualitative, because the actual transmission of the channels cannot simply be predicted from the LDOS. The conductance depends also on the overlap of the relevant orbitals and on non-local properties like the disorder in the contact region. As a counter example, Fig. 13 shows that also intervals of positive spin polarization can be found, although the density of states of the minority-spin component is usually higher than for the majority-spin component. This is particularly dramatic in the tunneling regime at the end of the breaking process, where for instance in Fig. 13 we see that a value of $P = +80\%$ is reached. Such a reversal of the spin polarization is due to the fact that the couplings between the d orbitals of the two Ni tips decrease much faster with distance than the corresponding s orbitals. As will be discuss further below, the result is typically a reduction of the minority-spin conductance and therefore a positive value of P.

We would like to point out that the contribution of the minority-spin component to the conductance is very sensitive to changes in the configuration. As is evident from Fig. 13, the minority spin shows stronger fluctuations than the majority spin as a function of the elongation. Again, this is a consequence of the fact that the minority-spin contribution is dominated by the d orbitals, which are anisotropic and therefore more susceptible to disorder than the s states responsible for the conductance of the majority spins. The sensitivity to atomic configurations is in agreement with the findings for Ag and Pt as discussed above, where stronger fluctuations of the conductance are seen for the transition metal Pt, as compared with the noble metal Ag.

B. Statistical analysis of nickel contacts

For the Ni contacts we did not observe the formation of any chain in the 50 simulated stretching processes. As a consequence, only a small first peak is visible in the MCS histogram (see Fig. 15). This peak originates from the dimer configurations, which usually form before the contacts break. In the conductance histogram there is a shoulder at around $1.3\,G_0$. Part of this first peak is buried under the subsequent conductance peak with its maximum at $2.5\,G_0$. This second very broad peak is mainly influenced by the starting configuration, which means that the small size of our contacts might hide part of the peak structure in the conductance histogram. According to the MCS regions contributing to the shoulder in the Ni conductance histogram, the first peak is mainly composed of thick contacts (MCS of around 2 Å). This also explains the large broadening of the histogram peak, since for thick contacts, there is more configurational variability.

Concerning the comparison with measurements, the shoulder at $1.3\,G_0$ in our results is in agreement with the experimental conductance histogram, where a particularly broad peak between $1.1\,G_0$ and $1.6\,G_0$ is observed.[80] Our calculations indicate that this peak contains contributions from high-MCS regions. The remarkable width of the first peak in the experimental conductance histogram is then explained by the configurational variability of thick contacts in conjunction with the contribution of configurationally sensitive d states to the conductance of the minority-spin component. However, this interpretation requires further discussion. Usually the first peak in the experimental conductance histograms is believed to arise from single-atom contacts and dimers.[7] With respect to the problems encountered for Al (cf. Sec. V), it may be that the employed EMT potential for Ni underestimates the stability of single-atom and dimer configurations in a similar manner. As a consequence the contri-

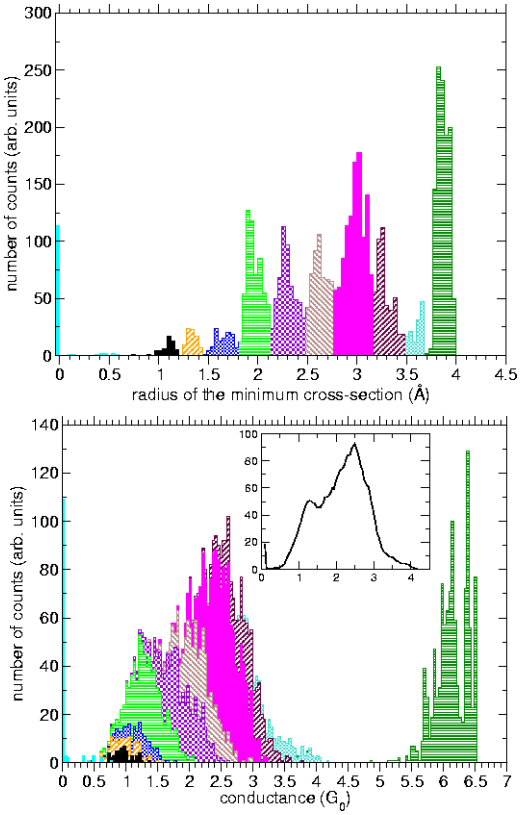

Figure 15: (Color online) MCS (minimum cross-section) histogram (upper panel) and conductance histogram (lower panel) for Ni (4.2 K, [001] direction, 50 contacts). In the MCS histogram different regions of frequently occurring radii have been defined with different pattern styles. The patterns in the conductance histogram indicate the number of counts for conductances belonging to the corresponding region of the MCS histogram. In the inset of the lower panel the conductance histogram is displayed in the relevant region in a smoothed version by averaging over six nearest-neighbor points.

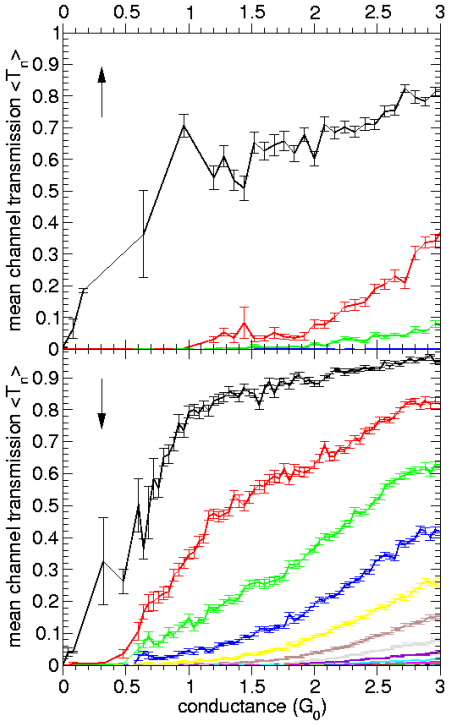

Figure 16: (Color online) Mean value of the transmission coefficient $\langle T_n^\sigma \rangle$ for the respective spin component σ as a function of the conductance for Ni (4.2 K, [001] direction, 50 contacts). The error bars indicate the mean error.[61]

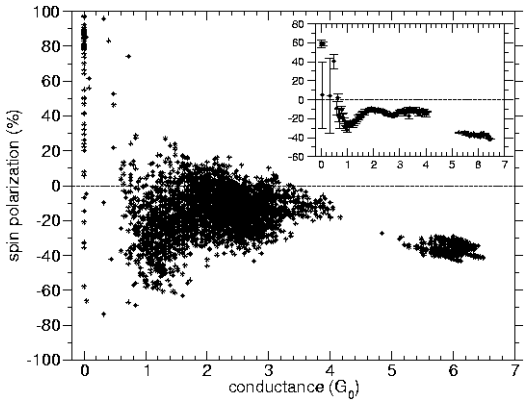

Figure 17: Spin polarization of the current as a function of the conductance. All the data points for the spin polarization are plotted in the graph, while in the inset their arithmetic mean and the corresponding mean error are displayed.[86]

bution of such configurations to the first peak in the conductance histogram may be underestimated in our calculations. In addition, as mentioned above, this first peak in the conductance histogram is not well separated from contributions with a high MCS, which are influenced by our starting configuration. Simulations of thicker contacts and more sophisticated calculations of the contact geometry may be needed to clarify the robustness of our findings.

Regarding to the mean channel transmission of the spin-components as a function of the conductance,[61] the minority-spin component exhibits more transmission channels than the majority-spin component (see Fig. 16). This further illustrates our previous argument, where we explained that the majority-spin component possesses an Ag-like character, while the minority-spin component behaves more Pt-like. Note also that the first channel for the majority-spin component opens up remarkably slowly compared with Ag (cf. Fig. 5).

Now we want to address the question of how the spin polarization of the current is influenced by configurational changes. For this purpose, we show in Fig. 17 the spin polarization P as a function of the conductance for all the 50 simulated breaking events. As it could already be observed in the simulation of a single breaking event (cf. Fig. 13), the spin polarization of all the contacts starts at a value of -40%, when the contact is close to its starting configuration. As explained above, this value for the spin polarization of the current coincides rather

well with the polarization of the bulk density of states at the Fermi energy. As the contact is stretched, also the diversity of geometrical configurations increases and the spin polarization values are widely spread, ranging from around -60% to 20%. There is a tendency towards negative spin polarizations, as can be observed in the inset of Fig. 17. The average spin polarization varies between -30% and -10% for conductances above $0.6\,G_0$. As described in the previous subsection, these variations arise from the high sensitivity of the minority-spin conductance to atomic positions, as compared to the less sensitive majority-spin conductance. The trend towards negative P values can be explained by the higher number of states present at the Fermi energy for the minority-spin component as opposed to the majority-spin component.

In the region of conductances below $0.6\,G_0$ the number of points is comparatively lower, which explains the partly bigger error bars. Nevertheless, the number of realizations is still enough to see the spreading of P values over an even wider interval than in the contact regime, together with an average tendency towards positive values. We attribute this trend of reversed spin polarizations to the faster radial decay of the hoppings between the d orbitals that dominate the minority-spin contribution to the conductance, as compared with the s orbitals that dominate majority-spin contribution. The faster decay with distance overcomes in the tunneling regime the effect of the higher density of states of the d bands versus the s bands.

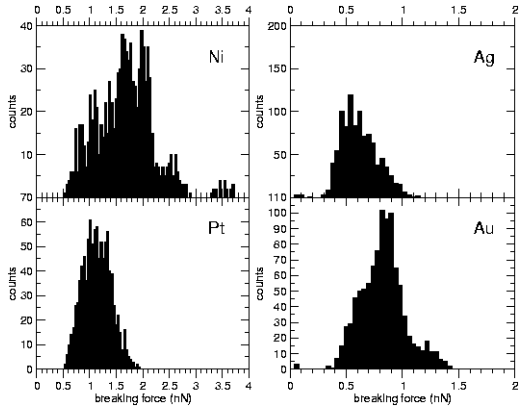

Figure 18: Histogram of the force needed to break atomic contacts of the metals Ag, Au, Pt and Ni. For every contact the highest 20 force values of the last 30 recorded geometries before the point of rupture are gathered. The force data for 50 contacts of the respective metal are assembled in the respective histograms.

metal	Ag	Au	Pt	Ni
EMT	0.40-0.75	0.55-1.00	0.80-1.45	1.00-2.15
bulk	0.57	0.85	1.31	0.89

Table I: Breaking forces in nN for the metals Ag, Au, Pt and Ni. The values in the column called "EMT" (effective medium theory) are read off from the force histograms in Fig. 18 and "bulk" refers to Eq. (A3).

VII. MECHANICAL PROPERTIES OF METALLIC ATOMIC CONTACTS

Experimentally it is possible to measure simultaneously the conductance and the strain force during the breaking of nanowires.[12] Special attention has been devoted to the force in the very last stage of the stretching process.[42] For this reason, we present in this section a detailed analysis of this breaking force for the different metals discussed above, including the results for Au of Ref. 37. In addition, the exotic atomic chain structures will be investigated further.

Using the 50 contacts that we have simulated for the different metals, we construct histograms of the breaking force in the following way: We consider the last 30 recorded atomic configurations before the point of rupture of the contact. Out of them the 20 highest values of the strain force are assembled in a force histogram, combining the data from all 50 contacts.[87] The breaking force histograms obtained for the different metals are shown in Fig. 18. For all elements, except for Ni, a clear maximum is visible in the center of a broad distribution of force values. We will address later, why Ni forms an exception in our simulations.

It is elucidating to compare the values of the breaking force obtained in the simulations with the corresponding forces in bulk. For this purpose, we use the "universal" binding energy function, suggested in Ref. 88, to get a rough estimate for the breaking force expected for a bulk bond (see Appendix A for details).

Values for the breaking forces are put together in Tab. I. The expression for the breaking force in Eq. (A3) needs to be considered as a rough estimate of the force needed to break a bulk-like bond. Concerning a comparison of this bulk estimate and the EMT results, it needs to be recalled that the EMT employed in the MD simulations considers by construction the experimentally verified increase of atomic bonding energies for low coordination.[39] Breaking forces for low-coordinated chains have been shown to be two to three times larger than bulk-like bonds and bond breaking may take place at distances well before the inflection point of the bulk estimate (cf. Appendix A).[41] Another difference is that the forces listed under "bulk" are estimates for breaking forces of a single bond. This is not necessarily the case for the result called "EMT". The EMT results are based on the stretching of the nanocontacts in our MD simulations. If the contact breaks while more than one atom resides in the MCS, several atomic bonds might be contributing to the breaking force of the contacts. This implies that the resulting force could be higher than the breaking force for a single bond.

For elements with a large peak in the MCS histogram at single-atom radii, like for the elements Au and Pt,

which form chains, usually the contacts break after the formation of a dimer or atomic chain. As a consequence, for Ag, Au and Pt single atomic bonds are probed in the EMT results. For all these elements, the force estimated from bulk considerations agrees surprisingly well with the EMT results. For Ni however, there is a discrepancy between the breaking force determined with EMT and the bulk prediction. We attribute this to the fact that its MCS histogram does not display a pronounced peak for dimer structures (cf. Fig. 15), indicating that Ni dimers are less stable than dimers of the other investigated metals (Ag, Au and Pt). On account of this the breaking force typically contains contributions from more than a single atomic bond, and is therefore higher than the force of the bulk estimate. The contributions of several bonds also explain the broad distribution without a clear maximum for Ni in Fig. 18.

The absolute values of our breaking forces in Tab. I need not be quantitative, as the investigations of Rubio-Bollinger *et al.*[42] show. While our EMT-breaking force for Au coincides well with their value of "around 1 nN", they found that DFT calculations are in better agreement with the experimentally measured breaking force of 1.5 nN.

Coinciding with the DFT-simulations by Bahn *et al.*[41] the ordering of breaking force strengths for the different metals as predicted by the bulk estimate is $F_{\mathrm{Ag}} < F_{\mathrm{Au}} < F_{\mathrm{Ni}} < F_{\mathrm{Pt}}$, where F_{x} is the breaking force for the material x. The EMT results modify this ordering slightly by interchanging Pt and Ni.

Before we conclude, we want to investigate the appearance and structural properties of the peculiar atomic chain structures in more detail. The general mechanism behind the chain formation during a stretching process is an increase in bond strength between low-coordinated atoms.[37,41,42,89] Independent of the metal under investigation, we observed that contacts in which an atomic chain has formed always break because of a bond rupture at the chain ends. The higher bond strength for low-coordinated atoms explains this phenomenon. Namely, the terminal atoms in the chain are connected with the thicker part of the contact, and possesses a higher coordination number than the other chain atoms. As a consequence the bonds at the chain ends are weaker than the bonds in the interior of the chain.[89]

We want to illustrate the mechanical properties of an atomic chain considering as example the Pt contact of Fig. 8. In Fig. 19 we plot the atomic displacements for this Pt contact projected onto the stretching direction (z axis) in the final elastic stage for elongations of $L_i = 1.37$ nm and $L_f = 1.49$ nm. The z-projected displacement is defined as $d_{z,j} = R_{z,j}(L_f) - R_{z,j}(L_i)$, where $R_{z,j}$ is the z-component of atom j, and L_f (L_i) is the final (initial) elongation. (Additionally we add an offset to $d_{z,j}$, such that the fourth layer in the lower electrode has zero displacement.) Due to the low coordination of the chain atoms and the associated higher bond strength as compared to interatomic bonds of the other atoms in the central part of the nanowire, the chain is expected to be particularly stable. For this reason the chain atoms should stay close to each other in a displacement plot during an elastic stage of stretching. Instead, most of the displacement should take place in the regions of more highly coordinated atoms in the central part of the nanowire. Exactly this is visible in Fig. 19. Note that a similar analysis has been performed by Rubio-Bollinger *et al.*[42] for a Au chain.

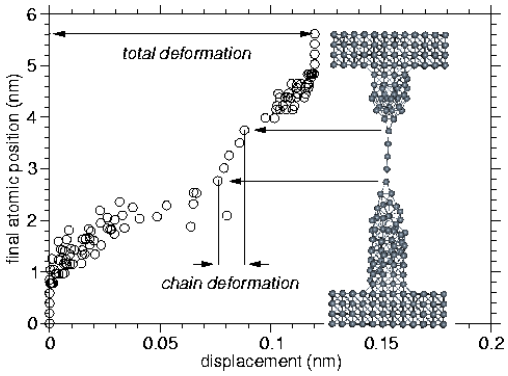

Figure 19: (Color online) The atomic displacements for the Pt contact of Fig. 8 are shown in the last elastic stage before rupture (change in coordinates between initial and final elongations of $L_i = 1.37$ nm and $L_f = 1.49$ nm). On the abscissa the displacement of each atom is plotted, while on the ordinate the positions of the atoms can be seen at the end of the elastic stage (elongation L_f). To the right the final configuration is displayed. The atomic displacements and positions have both been projected onto the stretching direction (z axis).

Finally, we want to comment on experimental results of Ref. 64. There, Smit *et al.* compare the tendency of formation of atomic chains for the neighboring $4d$ and $5d$ elements, namely Rh, Pd and Ag compared to Ir, Pt and Au. They find a higher occurrence of chains for the $5d$ elements as compared to $4d$ elements, and explain this by a competition between s and d bonding. From their data[90] we extract an enhancement factor of chain formation of 3.28 for Au compared to Ag. Taking the ratio between the content of the first MCS peak in the histograms, which corresponds to dimers and atomic chains, for Ag and Au normalized by the complete area of the MCS histograms (cf. Fig. 4 and Fig. 9 of Ref. 37), we obtain a value of 3.09, in good agreement with their experiments. Bahn *et al.*[41] pointed out that the chain formation depends sensitively on the initial atomic configuration. In general we believe that chain formation in our thin geometries might be enhanced compared to experimental conditions. Nevertheless the chain enhancement factor, as it is a relative measure, might be robust.

VIII. CONCLUSIONS

In summary, we have analyzed the mechanical and electrical properties of Ag, Pt and Ni nanojunctions. Using a combination of classical MD simulations and transport calculations based on a TB model supplemented with a local charge neutrality condition, we have studied the origin of the experimentally observed characteristic features in the conductance histograms of these metals. The ensemble of our results indicates that the peak structure of the low-temperature conductance histograms originates from an artful interplay between the mechanical properties and the electronic structure of the atomic-sized contacts.

We have found strong qualitative differences between these metals. In the case of Ag wires, we observe a first peak at $1\,G_0$ in the conductance histogram, resulting from single-atom contacts and dimers in good agreement with experiments.[55] In the last stages of the stretching process the transport is dominated by a single conduction channel, which arises mainly from the contribution of the $5s$ orbitals. We find practically no formation of monoatomic chains, as opposed to Au wires.[37] To be precise, the chain formation is found to be suppressed by a factor of three compared to Au, which is again consistent with the experimental observations.[64]

In the case of Pt contacts, the first peak in the conductance histogram is mainly due to single-atom contacts and long atomic chains. However, it also contains some contributions from contacts with larger MCS radii. This peak is rather broad and centered around $1.15\,G_0$, which is somewhat below the experimental value of $1.5\,G_0$.[55,63] The differences in width and value of this conductance peak, as compared with Ag, can be attributed to the key contribution of the $5d$ orbitals to the transport. First, the d orbitals provide additional conduction channels. Commonly there are three open transmission channels in the final stages of the Pt contacts. Second, these additional channels naturally give rise to higher conductance values. Third, caused by their spatial anisotropy the d orbitals are much more sensitive to changes in the contact geometry, which results in a larger width of the histogram features.

With respect to Al the statistical analysis of the contacts was hindered due to shortcomings in the employed EMT potential. However, for a sensible example a region of three transmitting channels is observed shortly before contact rupture, and the conductance of the dimer configuration is close to $1\,G_0$, which agrees nicely with experimental observations.[5] These three channels originate from the contribution of the partly occupied sp-hybridized valence orbitals of Al to the transport. In addition, our results reproduce the peculiar positive slopes of the last plateaus of the stretching curves.[5,6,34,71]

In the case of ferromagnetic Ni, we have shown that the contacts behave as a mixture of a noble metal (like Ag) and a transition metal (like Pt). While the $4s$ orbitals play the main role for the transport of the majority-spin electrons, the conduction of the minority-spin electrons is controlled by the partially occupied $3d$ orbitals. This follows from the position of the Fermi energy, which lies in the s band for the majority spins and in the d bands for the minority spins. In the conductance histogram we obtain a shoulder at $1.3\,G_0$, whose large width can again be attributed to the extreme sensitivity of the d orbitals to atomic configurations. On the other hand, we find that the spin polarization of the current in the Ni contacts is generally negative, increasing and fluctuating as the contacts narrow down and become disordered. In particular, large positive values are possible in the tunneling regime, right after the rupture of the wires. Once more, this behavior can be traced back to the fact that the d orbitals play a key role in the conductance of the minority-spin component.

The mechanical properties of our nanocontacts have been analyzed in detail with respect to breaking forces and the peculiar atomic chains. Concerning the breaking forces a simple estimate for the maximal force per bulk bond matches well the simulation results for Ag and Pt. However, Ni shows deviations from the bulk estimate and an extraordinarily broad distribution of breaking force values, which we attribute to the generally larger thickness of the contacts at the breaking point, meaning that the breaking force contains contributions of several atomic bonds. Contacts with an atomic chain configuration were observed to always tear apart due to a bond rupture at the chain ends in agreement with previous simulations.[89] Pt atomic chains were illustrated to exhibit an enhanced stability as compared to the remaining atoms in thicker parts of the nanowire.

Another important observation is that, although we obtain for every metal a sequence of peaks in the MCS (minimum cross-section) histogram, these peaks are smeared out in the conductance histograms. This indicates that not only the narrowest part of the constriction determines the conductance, but also the atomic configuration close to the narrowest part plays a role. This finding challenges the direct translation of peak positions in the conductance histogram into contact radii via the Sharvin formula. However, we should also point out the limitations of our modeling, in particular the small number of atoms present in the junctions. Moreover, let us remind that we have focused our analysis on low temperatures (4.2 K), where the atoms do not have enough kinetic energy to explore the low-energy configurations. Both the small number of atoms and the low temperature may cause an enhanced atomic disorder of the contacts in the stretching process.

The effects of higher temperatures, different crystallographic orientations of the contacts, other protocols of the stretching process with different annealing, heating and relaxation times have not been addressed in this study. A first-principles description of thick contacts, in which both the mechanics and the electronic structure of the contacts are treated at a higher level of accuracy and on an equal footing, should be a major goal for the theory

in the future. Experiments in which, simultaneously to the recording of a conductance histogram, also the contact geometries are observed, could help to validate the correlation between conductance peaks and stable wire radii.

IX. ACKNOWLEDGMENTS

We thank E. Scheer, Gerd Schön and R.H.M. Smit for helpful discussions. FP, JKV, MH and JCC were supported financially by the Landesstiftung Baden-Württemberg within the "Kompetenznetz Funktionelle Nanostrukturen", the Helmholtz Gemeinschaft within the "Nachwuchsgruppen-Programm" (Contract No. VH-NG-029) and the DFG within the CFN. The granting of computer time at the Institut für Nanotechnologie (Forschungszentrum Karlsruhe) is gratefully acknowledged. MD and PN appreciate the support by the SFB 513 and granting of computer time from the NIC, the SSC and the HLRS.

Appendix A: BULK FORCE

We give here a short derivation of an estimate for the force needed to break a bulk-like bond in a fcc lattice (cf. Eq. (A3)). The reasoning follows Ref. 42 (see remark [25] of that Ref.), where however no derivation is given.

The total energy of a crystal can approximately be written as $E_N(r) = NE(r)$, where N is the number of atoms in the volume V of the considered crystal, $E(r) = E_{\rm coh}E^*(r^*)$ is the energy of a single atom as a function of the Wigner-Seitz radius, $E_{\rm coh}$ is the equilibrium cohesive energy (or enthalpy of formation) and $E^*(r^*)$ is the "universal" energy function $E^*(r^*) = -(1+r^*)\exp(-r^*)$.[88] The Wigner-Seitz radius r is defined as $r = (3/4\pi n_A)^{1/3}$ with the atom density n_A. Because $n_A = N/V = 4/a^3$ in a fcc crystal, r is connected with the fcc-lattice constant a via $r = (3/16\pi)^{1/3}\, a$. Additionally, $r^* = (r - r_0)/\ell$ is the scaled Wigner-Seitz radius and r_0 the equilibrium value of r. The length scale ℓ is related to the bulk modulus B, and it can be shown[88] that

$$\ell = \sqrt{\frac{E_{\rm coh}}{12\pi B r_0}} = \left(\frac{16\pi}{3}\right)^{\frac{1}{6}} \sqrt{\frac{E_{\rm coh}}{12\pi B a_0}} \qquad \text{(A1)}$$

with the equilibrium fcc-lattice constant a_0.

An estimate for the maximal force F needed to break a bulk-like bond may be obtained at the the inflection point of $E_N(r)$ at a Wigner-Seitz radius $r_{\rm ip} = r_0 + \ell$ (where ip stands for inflection point). If we use the relation $r = (3/16\pi)^{1/3}\sqrt{2}x$ between the Wigner-Seitz radius and the fcc-nearest-neighbor distance (or interatomic bond length) x, an approximate bond length at rupture of $x_{\rm ip} = (a_0 + (16\pi/3)^{1/3}\,\ell)/\sqrt{2}$ is obtained. The absolute value of the maximal force F per bond (where there are $6N$ bonds in a fcc lattice) is then given as

$$F = \frac{1}{6N}\left.\frac{d\tilde{E}_N(x)}{dx}\right|_{x=x_{\rm ip}} = \left(\frac{3}{16\pi}\right)^{\frac{1}{3}} \frac{\sqrt{2}E_{\rm coh}}{6\exp(1)\,\ell}. \qquad \text{(A2)}$$

(where $\tilde{E}_N(x) = E_N(r)$). This finally leads to the following maximal force per bond in a fcc lattice:

$$F = \sqrt{\frac{E_{\rm coh}Ba_0}{8\exp(2)}}. \qquad \text{(A3)}$$

In order to obtain numerical values from Eq. (A3), we employ the data listed in Ref. 91 for the three constants $E_{\rm coh}$, B and a_0.

* Electronic address: Fabian.Pauly@tfp.uni-karlsruhe.de

[1] N. Agraït, A. Levy Yeyati, J.M. van Ruitenbeek, Phys. Rep. **377**, 81 (2003).
[2] N. Agraït, J.G. Rodrigo, S. Vieira, Phys. Rev. B **47**, 12345 (1993).
[3] J.I. Pascual, J. Méndez, J. Gómez-Herrero, A.M. Baró, N. García, V.T. Binh, Phys. Rev. Lett. **71**, 1852 (1993).
[4] C.J. Muller, J.M. van Ruitenbeek, L.J. de Jongh, Physica C **191**, 485 (1992).
[5] E. Scheer, P. Joyez, D. Esteve, C. Urbina, M.H. Devoret, Phys. Rev. Lett. **78**, 3535 (1997).
[6] J.C. Cuevas, A.L. Yeyati, A. Martín-Rodero, Phys. Rev. Lett. **80**, 1066 (1998).
[7] E. Scheer, N. Agraït, J.C. Cuevas, A. Levy Yeyati, B. Ludoph, A. Martín-Rodero, G.R. Bollinger, J.M. van Ruitenbeek, C. Urbina, Nature **394**, 154 (1998).
[8] J.C. Cuevas, A. Levy Yeyati, A. Martín-Rodero, G.R. Bollinger, C. Untiedt, N. Agraït, Phys. Rev. Lett. **81**, 2990 (1998).
[9] L. Olesen, E. Lægsgaard, I. Stensgaard, F. Besenbacher, J. Schiøtz, P. Stoltze, K.W. Jacobsen, J.K. Nørskov, Phys. Rev. Lett. **74**, 2147 (1995).
[10] J.M. Krans, J.M. van Ruitenbeek, V.V. Fisun, I.K. Yanson, L.J. de Jongh, Nature **375**, 767 (1995).
[11] Z. Gai, Y. He, H. Yu, W.S. Yang, Phys. Rev. B **53**, 1042 (1996).
[12] N. Agraït, G. Rubio, S. Vieira, Phys. Rev. Lett. **74**, 3995 (1995).
[13] A.I. Yanson, I.K. Yanson, J.M. van Ruitenbeek, Nature **400**, 144 (1999).
[14] A.I. Yanson, I.K. Yanson, J.M. van Ruitenbeek, Phys. Rev. Lett. **87**, 216805 (2001).
[15] E. Medina, M. Díaz, N. León, C. Guerrero, A. Hasmy, P.A. Serena, J.L. Costa-Krämer, Phys. Rev. Lett. **91**, 026802 (2003).
[16] A.I. Mares, A.F. Otte, L.G. Soukiassian, R.H.M. Smit, J.M. van Ruitenbeek, Phys. Rev. B **70**, 073401 (2004).
[17] A.I. Mares, J.M. van Ruitenbeek, Phys. Rev. B **72**, 205402

(2005).
[18] V. Rodrigues, T. Fuhrer, D. Ugarte, Phys. Rev. Lett. **85**, 4124 (2000); V. Rodrigues, D. Ugarte, Phys. Rev. B **63**, 073405 (2001).
[19] Y. Kondo, K. Takayanagi, Science **289**, 606 (2000).
[20] Y. Oshima, H. Koizumi, K. Mouri, H. Hirayama, K. Takayanagi, Y. Kondo, Phys. Rev. B **65**, 121401(R) (2002).
[21] J.A. Torres, J.I. Pascual, J.J. Sáenz, Phys. Rev. B **49**, 16581 (1994).
[22] Hard wall boundaries are assumed in this formula, and the inclusion of a work function alters the prefactor of the second term as explained in A. García-Martín, J.A. Torres, J.J. Sáenz, Phys. Rev. B **54**, 13448 (1996). This effect is usually not taken into account.
[23] A. Hasmy, E. Medina, P.A. Serena, Phys. Rev. Lett. **86**, 5574 (2001).
[24] U. Landman, W.D. Luedtke, N.A. Burnham, R.J. Colton, Science **248**, 454 (1990).
[25] A.P. Sutton, J.B. Pethica, J. Phys.: Condens. Matter **2**, 5317 (1990).
[26] T.N. Todorov, A.P. Sutton, Phys. Rev. Lett. **70**, 2138 (1993).
[27] A.M. Bratkovsky, A.P. Sutton, T.N. Todorov, Phys. Rev. B **52**, 5036 (1995).
[28] T.N. Todorov, A.P. Sutton, Phys. Rev. B **54**, R14234 (1996).
[29] H. Mehrez, S. Ciraci, Phys. Rev. B **56**, 12632 (1997).
[30] M. Brandbyge, M.R. Sørensen, K.W. Jacobsen, Phys. Rev. B **56**, 14956 (1997).
[31] A. Buldum, S. Ciraci, I.P. Batra, Phys. Rev. B **57**, 2468 (1998).
[32] M.R. Sørensen, M. Brandbyge, K.W. Jacobsen, Phys. Rev. B **57**, 3283 (1998).
[33] A. Nakamura, M. Brandbyge, L.B. Hansen, K.W. Jacobsen, Phys. Rev. Lett. **82**, 1538 (1999).
[34] P. Jelínek, R. Pérez, J. Ortega, F. Flores, Phys. Rev. B **68**, 085403 (2003).
[35] E.Z. da Silva, F.D. Novaes, A. J. R. da Silva, A. Fazzio, Phys. Rev. B **69**, 115411 (2004).
[36] J.A. Torres, J.J. Sáenz, Phys. Rev. Lett. **77**, 2245 (1996); T. López-Ciudad, A. García-Martín, A.J. Caamaño, J.J. Sáenz, Surf. Sci. **440**, L887 (1999); J. Bürki, C.A. Stafford, X. Zotos, D. Baeriswyl, Phys. Rev. B **60**, 5000 (1999); A. García-Martín, M. del Valle, J.J. Sáenz, J.L. Costa-Krämer, P.A. Serena, Phys. Rev. B **62**, 11139 (2000).
[37] M. Dreher, F. Pauly, J. Heurich, J.C. Cuevas, E. Scheer, P. Nielaba, Phys. Rev. B **72**, 075435 (2005).
[38] A. Hasmy, A.J. Pérez-Jiménez, J.J. Palacios, P. García-Mochales, J.L. Costa-Krämer, M. Díaz, E. Medina, P.A. Serena, Phys. Rev. B **72**, 245405 (2005).
[39] K.W. Jacobsen, P. Stoltze, J.K. Nørskov, Surf. Sci. **366**, 394 (1996).
[40] P. Stoltze, Simultion methods in atomic-scale materials physics, Polyteknisk Forlag, 1997: page 258.
[41] S.R. Bahn, K.W. Jacobsen, Phys. Rev. Lett. **87**, 266101 (2001).
[42] G. Rubio-Bollinger, S.R. Bahn, N. Agraït, K.W. Jacobsen, S. Vieira, Phys. Rev. Lett. **87**, 026101 (2001).
[43] G.M. Finbow, R.M. Lynden-Bell, I.R. McDonald, Molecular Physics **92**, 705 (1997).
[44] Note that the overlap elements $S_{i\alpha,j\beta}$ are spin-independent for all the metals studied in this work. In principle, the formulation of the employed TB parameterization allows a spin-dependence of the overlap integrals for ferromagnetic metals,[45] but for the parameters used for Ni,[46] they are identical for the different spin-components. This is expected, because the elements of the overlap matrix $S_{i\alpha,j\beta}$ should just be integrals over some (real) basis functions ϕ with orbital indices α and β at atomic positions $\mathbf{R}_i$ and $\mathbf{R}_j$ ($S_{i\alpha,j\beta} = \int \phi_\alpha(\mathbf{r}-\mathbf{R}_i)\phi_\beta(\mathbf{r}-\mathbf{R}_j)d^3r$).
[45] M.J. Mehl, D.A. Papaconstantopoulos, Phys. Rev. B **54**, 4519 (1996); "Tight-Binding Parametrization of First-Principles Results" in Computational Materials Science, C. Fong, ed. (World Scientific Publishing, Singapore, 1998); http://cst-www.nrl.navy.mil/bind/.
[46] See parameters ni_ferro_par at http://cst-www.nrl.navy.mil/bind/ni.html; M.I. Haftel, N. Bernstein, M.J. Mehl, D.A. Papaconstantopoulos, Phys. Rev. B **70**, 125419 (2004).
[47] Technically the integration runs along a semicircular contour in the upper complex plane.[92] The lower end of the contour starts at $-5\,\mathrm{Ry} = -68\,\mathrm{eV}$, well below all orbital energies, and ends at the Fermi energy of the respective metal. The integration points (around 150) have once been determined for a thin configuration of an exemplary contact of each metal with the help of an adaptive integration scheme of the closed Newton-Cotes form.[93] But to speed up the iterative determination of the charge neutral Hamiltonian elements, which takes the most computer time in our computations, the points are kept unchanged in later integrations. The integration points get denser, when the Fermi energy is reached. The imaginary offset from the real axis is 10^{-4} Ry, and has been checked to be sufficiently small to insure converged conductance results.
[48] The circumstance that for simplicity matrices only extend over the central part of our system and charges in the electrodes are neglected has a slight influence on the conductance for thick contacts due to interface effects. But during the stretching process, the narrowest part of the junction plays an ever more important role, so that finally this approximation becomes unimportant.
[49] The Mulliken population analysis $N_i = \sum_\alpha (PS)_{i\alpha,i\alpha}$ is chosen over the Löwdin analysis $N_i = \sum_\alpha (S^{1/2}PS^{1/2})_{i\alpha,i\alpha}$, which would be more consistent with the LDOS calculation (cf. Eq. (12)) due to efficiency reasons. First the square root of the overlap does not need to be computed in the Mulliken population analysis. But the main advantage is the saving of an additional matrix multiplication required in every step of the iterative solution of the charge-neutrality condition, which requires that $|N_i - N_{\mathrm{atom}}| < 0.02$ for every atom i of the central part of the nanowire.
[50] M. Brandbyge, N. Kobayashi, M. Tsukada, Phys. Rev. B **60**, 17064 (1999).
[51] The averaged transmission $\langle T \rangle$ (cf. Eq. (11)) is determined as a sum over $T(E)$ on 11 equally spaced points in the energy interval $[E_F - \Delta, E_F + \Delta]$ around the Fermi energy ($\Delta = 50$ meV).
[52] A. Szabo, N.S. Ostlund, Modern Quantum Chemistry: Introduction to Advanced Electronic Structure Theory, Dover 1996.
[53] For plots of the LDOS of an atom a broadening of $\eta = 10^{-3}\,\mathrm{Ry} = 0.0136\,\mathrm{eV}$ is used in $\hat{G}_{CC,\sigma}$ (cf. Eq. (4)), while for transport the broadening is chosen to be $\eta = 10^{-8}\,\mathrm{Ry} = 1.36 \cdot 10^{-7}\,\mathrm{eV}$.
[54] B. Ludoph, J.M. van Ruitenbeek, Phys. Rev. B **61**, 2273

(2000).
[55] A.I. Yanson, Ph.D. thesis, Universiteit Leiden, The Netherlands, 2001.
[56] V. Rodrigues, J. Bettini, A.R. Rocha, L.G.C. Rego, D. Ugarte, Phys. Rev. B **65**, 153402 (2002).
[57] For the division of a conductance trace into regions with different numbers of open conductance channels we use a criterion of $T_n^\sigma < 0.01$ to consider the nth channel to be closed. This division is only approximate: Due to fluctuations in the geometry, a channel transmission may fall temporarily below 0.01 but reenter later on. In other cases (especially Pt, Al and Ni) many channels are present and, in order not to overload our pictures, we need to combine several channel-closing events into one.
[58] J.L. Mozos, P. Ordejón, M. Brandbyge, J. Taylor, K. Stokbro, Nanotechnology **13**, 346 (2002).
[59] Y.J. Lee, M. Brandbyge, M.J. Puska, J. Taylor, K. Stokbro, R.M. Nieminen, Phys. Rev. B **69**, 125409 (2004).
[60] I.K. Yanson, O.I. Shklyarevskii, Sz. Csonka, H. van Kempen, S. Speller, A.I. Yanson, J.M. van Ruitenbeek, Phys. Rev. Lett. **95**, 256806 (2005).
[61] The mean channel transmission $\langle T_n^\sigma \rangle$ as a function of the conductance is determined as follows: For all simulated contacts of a certain metal we consider the breaking curve of the conductance and all the channel transmissions T_n^σ. (For the nonferromagnetic contacts we suppress the spin index σ in this article.) Next we concentrate on a fixed conductance $G = G^\uparrow + G^\downarrow$ (within a bin-width of $0.04\,G_0$). We obtain the mean channel transmission $\langle T_n^\sigma \rangle$ of the nth channel as the mean value over all the corresponding individual channel transmissions $T_{n,j}^\sigma$ for this fixed conductance ($\langle T_n^\sigma \rangle = \sum_{j=1}^{N} T_{n,j}^\sigma / N$, where N is the number of values present in the average). The error of the mean channel transmission (as given in Figs. 5, 11 and 16) is computed as the mean error of the arithmetic mean $\chi = 0.8\widetilde{\sigma}/\sqrt{N}$ and $\widetilde{\sigma} = \sqrt{\sum_j \left(T_{n,j}^\sigma - \langle T_n^\sigma \rangle\right)^2 / N\,(N-1)}$ is the mean quadratic error of the values $T_{n,j}^\sigma$.[94] (The average $\langle T_n \rangle$ should not to be confused with the average over energies employed to determine $\langle G \rangle$ (cf. Eq. (11)).)
[62] B. Ludoph, M.H. Devoret, D. Esteve, C. Urbina, J.M. van Ruitenbeek, Phys. Rev. Lett. **82**, 1530 (1999).
[63] R.H.M. Smit, Y. Noat, C. Untiedt, N.D. Lang, M.C. van Hemert, J.M. van Ruitenbeek , Nature **419**, 906 (2002).
[64] R.H.M. Smit, C. Untiedt, A.I. Yanson, J.M. van Ruitenbeek, Phys. Rev. Lett. **87**, 266102 (2001).
[65] R.H.M. Smit, C. Untiedt, G. Rubio-Bollinger, R.C. Segers, J.M. van Ruitenbeek, Phys. Rev. Lett. **91**, 076805 (2003).
[66] L. de la Vega, A. Martín-Rodero, A.L. Yeyati, A. Saúl, Phys. Rev. B **70**, 113107 (2004).
[67] S.K. Nielsen, M. Brandbyge, K. Hansen, K. Stokbro, J.M. van Ruitenbeek, F. Besenbacher, Phys. Rev. Lett. **89**, 066804 (2002).
[68] S.K. Nielsen, Y. Noat, M. Brandbyge, R.H.M. Smit, K. Hansen, L.Y. Chen, A.I. Yanson, F. Besenbacher, J.M. van Ruitenbeek, Phys. Rev. B **67**, 245411 (2003).
[69] V.M. García-Suárez, A.R. Rocha, S.W. Bailey, C.J. Lambert, S. Sanvito, J. Ferrer, Phys. Rev. Lett. **95**, 256804 (2005).
[70] Further investigations are needed to find out, why the transmission of dimers and short chains is rather $1\,G_0$ than $1.5\,G_0$. Possible reasons could lie in the structural properties, like for example the high disorder of our thin contacts or linear instead of zigzag chains. The approximation of surface Green's functions by bulk Green's functions in the electrodes has been checked to have little influence on the transmission when chains have formed. Potentially the low transmission for dimers and short chains could also indicate limitations for the use of the Pt TB parameters in conductance calculations.
[71] J.M. Krans, C.J. Muller, I.K. Yanson, Th.C.M. Govaert, R. Hesper, J.M. van Ruitenbeek, Phys. Rev. B **48**, 14721 (1993).
[72] A. I. Yanson, J.M. van Ruitenbeek, Phys. Rev. Lett. **79**, 2157 (1997).
[73] T. Kitamura, Y. Umeno, Modelling Simul. Mater. Sci. Eng. **11**, 127 (2003).
[74] J.L. Costa-Krämer, Phys. Rev. B **55**, R4875, (1997).
[75] F. Ott, S. Barberan, J.G. Lunney, J.M.D. Coey, P. Berthet, A.M. de Leon-Guevara, A. Revcolevschi, Phys. Rev. B **58**, 4656 (1998).
[76] T. Ono, Y. Ooka, H. Miyajima, Y. Otani, Appl. Phys. Lett. **75**, 1622 (1999).
[77] M. Viret, S. Berger, M. Gabureac, F. Ott, D. Olligs, I. Petej, J.F. Gregg, C. Fermon, G. Francinet, G. LeGoff, Phys. Rev. B **66**, 220401(R) (2002).
[78] F. Elhoussine, S. Mátéfi-Tempfli, A. Encinas, L. Piraux, Appl. Phys. Lett. **81**, 1681 (2002).
[79] V. Rodrigues, J. Bettini, P.C. Silva, D. Ugarte, Phys. Rev. Lett. **91**, 096801 (2003).
[80] C. Untiedt, D.M.T. Dekker, D. Djukic, J.M. van Ruitenbeek, Phys. Rev. B **69**, 081401(R) (2004).
[81] More generally, the half-integer conductance quantization could also arise from a perfectly polarized current, where the channel transmissions of the transmitted spin-component add up to one.
[82] A. Martín-Rodero, A. Levy Yeyati, J.C. Cuevas, Physica C **352**, 67 (2001).
[83] A. Delin, E. Tosatti, Phys. Rev. B **68**, 144434 (2003).
[84] A. Bagrets, N. Papanikolaou, I. Mertig, Phys. Rev. B **70**, 064410 (2004).
[85] D. Jacob, J. Fernández-Rossier, J.J. Palacios, Phys. Rev. B **71**, 220403(R) (2005).
[86] Note that bins (where a of bin-width of $0.04\,G_0$ has been used) containing only a single data point are not displayed in the inset of Fig. (17). The reason is that the calculation of the mean error of the arithmetic mean requires at least two data points.[61]
[87] The choice of the 20 highest force values out of the last 30 recorded geometries before the point of rupture for each of the 50 simulated contacts can be justified as follows: To obtain enough statistics on the breaking force, and because of the evident fluctuations in the strain force (cf. Fig (2), for example) several geometries after breaking of a wire need to be considered in the breaking force histogram. This is why we take into account 30 recorded geometries before the point of rupture. However, the very tiny strain forces directly after and at the point of rupture (which is signaled by a negligible MCS of less than 0.3 Å) will produce artificial peaks at small force values. For this reason we select the 20 highest strain forces from the set of the 30 strain force values. This is done for each of the 50 simulated contacts, and the data is complied in the histogram of the breaking force.
[88] M.M. Sigalas, J.H. Rose, D.A. Papaconstantopoulos, H.B. Shore, Phys. Rev. B **58**, 13438 (1998); J.H. Rose, J.R. Smith, J. Ferrante, Phys. Rev. B **28**, 1835 (1983).
[89] S.R. Bahn, Ph.D. thesis, Technical University of Denmark,

Lyngby, 2001.
[90] In Fig. 4 of Ref. 64 a fraction of long plateaus is given for Au and Ag respectively. Taking the ratio between the $P_{1.5}$-values for Au and Ag, an enhancement of chains by a factor of $P_{1.5}(\mathrm{Au})/P_{1.5}(\mathrm{Ag}) \approx 0.59/0.18 = 3.28$ is found for Au compared to Ag.
[91] Ch. Kittel, Introduction to solid state physics <dt.>, Oldenbourg 1999.
[92] R. Zeller, J. Deutz, P.H. Dederichs, Solid State Comm. **44**, 993 (1982).
[93] W.H. Press, B.P. Flannery, S.A. Teukolsky, Numerical Recipes in FORTRAN 77 and FORTRAN 90: The Art of Scientific and Parallel Computing, Cambridge University Press, 1996.
[94] I.N. Bronstein, K.A. Semendjajew, G. Musiol, H. Mühling, Taschenbuch der Mathematik, Verlag Harri Deutsch 1997.